REPUBLIC OF TURKEY
ADANA ALPARSLAN TÜRKEŞ SCIENCE AND TECHNOLOGY UNIVERSITY

GRADUATE SCHOOL OF NATURAL AND APPLIED SCIENCES
DEPARTMENT OF BIOENGINEERING

Ab-initio Modeling of Co-based Water Reduction Catalysts in Aqueous Solution and on Surface

İpek GÜÇLÜ
MASTER OF SCIENCE

SUPERVISOR
Assoc. Prof. Yeliz GÜRDAL DURĞUN

ADANA YEAR

REPUBLIC OF TURKEY
ADANA ALPARSLAN TÜRKEŞ SCIENCE AND TECHNOLOGY UNIVERSITY

GRADUATE SCHOOL OF NATURAL AND APPLIED SCIENCES
DEPARTMENT OF BIOENGINEERING

Ab-initio Modeling of Co-based Water Reduction Catalysts in Aqueous Solution and on Surface

İpek GÜÇLÜ
MASTER OF SCIENCE

SUPERVISOR
Assoc. Prof. Yeliz GÜRDAL DURĞUN

ADANA, 2022

Ab-initio Modeling of Co-based Water Reduction Catalysts in Aqueous Solution and on Surface

submitted by **İpek GÜÇLÜ** in partial fulfillment of the requirements for the degree of **Master of Science in Department of Bioengineering, Adana Alparslan Türkeş Science and Technology University** by,

Assoc. Prof. Dr. Ahmet BEYCİOĞLU
Graduate School Director

Prof. Dr. Gözde BAYDEMİR PEŞİNT
Department Chair

Assoc. Prof. Dr. Yeliz GÜRDAL DURĞUN
Supervisor

Thesis Committee

Assoc. Prof. Dr. Yeliz GÜRDAL DURĞUN
Adana Alparslan Türkeş Science and Technology University

Asst. Prof. Dr. Ceyla ÖZGÜR
Adana Alparslan Türkeş Science and Technology University

Asst. Prof. Dr. Ersan EYİLER
Çukurova University

Thesis Defense Date

28/07/2022

I hereby declare that all information in this thesis has been obtained and presented in accordance with academic rules and ethical conduct. I also declare that, as required by these rules and conduct, I have fully cited and referenced all information that is not original to this work.

[Signature]

İpek GÜÇLÜ

ABSTRACT

Ab-initio Modeling of Co-based Water Reduction Catalysts in Aqueous Solution and on Surface

İpek GÜÇLÜ
Department of Bioengineering
Supervisor: Assoc. Prof. Dr. Yeliz GÜRDAL DURĞUN
July 2022, 61 pages

The common use of hydrogen as a renewable energy source has been one of today's challenges that, if resolved, could replace dependence on fossil fuels. One of the sustainable ways of H_2 production is the photocatalytic water reduction reaction catalyzed by molecules with transition metals as reaction centers. Studies have shown that cobalt-based catalysts have an active and efficient effect in photocatalytic water reduction reactions and can be used instead of expensive transition metals such as ruthenium and platinum. In this study, we investigate Co-based water reduction catalysts in aqueous solution as well as on the TiO_2 surface by means of Ab-initio Molecular Dynamics (AIMD), Metadynamics (MTD), Density Functional Theory (DFT) as well as Free Energy Perturbation Theory. Regarding homogeneous catalysis, we model the first and second electron injection intermediate steps of the EECC water reduction reaction mechanism. We analyze the solvent response following the electron injections as well as the behavior of the planar structure of the catalyst in the water solvent. The first and the second reduction free energies are calculated, AIMD trajectories are analyzed, and electronic structures of the selected snapshots are further evaluated using more sophisticated methods. For the heterogeneous catalysis, we compare the optimized geometries as well as adsorption energies of several cobalt-based catalysts on the rutile(110) surface. Electronic structures of the selected catalysts/TiO_2 systems are further investigated by calculating electron density difference maps.

Keywords: Ab-initio Molecular Dynamics, Density Functional Theory, Cobalt-Bipyridine Based Catalysts, Water Reduction Reaction, Free Energy Perturbation Theory

ÖZET

Kobalt-bazlı Su İndirgeme Katalizörlerinin Sulu Çözeltilerde ve Yüzeyde Ab-initio Moleküler Dinamik Yöntemi ile Modellenmesi

İpek GÜÇLÜ
Biyomühendislik Anabilim Dalı
Danışman: Doç. Dr. Yeliz GÜRDAL DURĞUN
Temmuz 2022, 61 sayfa

Hidrojen enerjisi yenilenebilir enerji kaynağı olarak fosil yakıtlara olan bağımlılığın yerini alabilir, dolayısıyla yaygın kullanımının arttırılması için çözüm arayışı günümüzün zorluklarından birini oluşturmuştur. H_2'nin sürdürülebilir üretim yöntemlerinden biri geçiş metallerine sahip moleküler katalizörler ile fotokatalitik su indirgeme reaksiyonudur. Çalışmalar, kobalt bazlı katalizörlerin fotokatalitik su indirgeme reaksiyonlarında aktif ve verimli bir etkiye sahip olduğunu ve Rutenyum ve Platin gibi pahalı geçiş metalleri yerine kullanılabileceğini göstermiştir. Bu çalışmada, Ab-initio Moleküler Dinamik (AIMD), Metadinamik (MTD), Yoğunluk Fonksiyoneli Teorisi (DFT) ve ayrıca Serbest Enerji Pertürbasyon Teorisi aracılığıyla hem sulu çözeltide hem de TiO_2 yüzeyinde Co bazlı su indirgeme katalizörlerinin çözelti veya yüzey ile etkileşimleri araştırılmıştır. Homojen katalizlenme ile ilgili olarak, EECC su indirgeme reaksiyon mekanizmasının birinci ve ikinci indirgeme ara adımları modellenmiştir. Elektron enjeksiyonlarını takiben çözücü tepkisi ve çözücüdeki katalizörün düzlemsel yapısı analiz edilmiştir. Birinci ve ikinci indirgenme serbest enerjileri hesaplanmış, AIMD yörüngeleri analiz edilmiş, ve yörüngelerden seçilen anlık görüntülerin elektronik yapıları daha karmaşık yöntemler kullanılarak ayrıca değerlendirilmiştir. Heterojen katalizlenme için, rutil(110) yüzeyinde birkaç kobalt bazlı katalizörün adsorpsiyon enerjilerinin yanı sıra optimize edilmiş geometrileri karşılaştırılmıştır. Seçilen katalizör/TiO_2 sistemlerinin elektronik yapıları, elektron yoğunluk farkı haritaları hesaplanarak ayrıca araştırılmıştır.

Anahtar Kelimeler: Ab-initio Moleküler Dinamik, Yoğunluk Fonksiyoneli Teorisi, Kobalt-Bipiridin Bazlı Katalizörler, Su İndirgeme Reaksiyonu, Serbest Enerji Pertürbasyon Teorisi

dedication

to myself in future

do everything you have to do, do everything with a good heart

and

live for yourself

ACKNOWLEDGEMENTS

I would like to express my deep and sincere gratitude to my research supervisor, Assoc. Prof. Yeliz Gürdal Durğun for giving me the opportunity to do research and providing invaluable guidance throughout this research. Her dynamism, vision, sincerity and motivation have deeply inspired me. She has taught me the methodology to carry out the research and to present the research works as clearly as possible. It was a great privilege and honor to work and study under her guidance. I am extremely grateful for what she has offered me. I would also like to thank her for her friendship, empathy, and great sense of humor. I am extending my heartfelt thanks to her family for their acceptance and patience during the discussion I had with her on research work and thesis preparation.

I would like to acknowledge the Scientific and Technological Research Council of Turkey (TUBITAK). This study has received funding from the TUBITAK under the 3501 Career Development Program (grant agreement No: 120Z240). The calculations reported in this thesis have been performed at the TUBITAK ULAKBIM, High Performance and Grid Computing Center (TRUBA), based in Turkey.

I would like to say thanks to my Molecular Modeling Research Group for their knowledges and supports. I express my special thanks to my lovely project colleague Ayas Kiser who encouraged me by saying that we will achieve that too whenever I get desperate, and to my dear cheerful friend Tuğçe Gökdemir who always make my day positive with her laughter even in my saddest moment.

I would like to thanks my special friend Özlem Dizidar Avcı who always be with me, share all my feelings since I was child and her little miracle. You are the most perfect news that I have been heard in this year. Come with your health and all beauty my little baby.

I thank the ATÜ Latino Dance Group, where I experienced the team spirit with a show where we were enchanted by the rhythm on the stage, one of the moments where I felt the most free and proud in my life.

I am extremely grateful to my beloved parents, Davut and Servet Güçlü for their love, prayers, caring and sacrifices for educating and preparing me for my future. You always believed in me for my success. Thank you so much.

TABLE OF CONTENTS

LIST OF FIGURES

LIST OF TABLES

NOMENCLATURE

Co	: Cobalt
Pt	: Platinium
H_2	: Hydrogen
CO_2	: Carbon dioxide
TiO_2	: Titanium dioxide
DFT	: Density Functional Theory
AIMD	: Ab-initio Molecular Dynamics
PBE	: Perdew-Burke Ernzerhof's
GTH	: Goedecker–Teter–Hutter
CSVR	: Canonical Sampling Through Velocity Rescaling
GGA	: General Gradient Approximation
ADMM	: Auxiliary Density Matrix Method
rVV-10	: Vydrov-Voorhis
DZVP	: Double-zeta Valence Plus Polarization
(GPW)	: Gaussian and plane wave
HOMO	: The Highest Occupied Molecular Orbital
LUMO	: The Lowest Unoccupied Molecular Orbital
CV	: Collective Variable
FES	: Free Energy Surface
WRC	: Water Reduction Catalyst
ρ	: Density
Å	: Angstrom
E	: Energy
E_{xc}	: Exchange-correlation Energy
T_s	: Non-interacting System's Kinetic Energy
J	: Classical Coulomb Repulsion energy

$E_{adsorption}$: Adsorption Energy

$E_{complex}$: Complex Energy

E_{slab} : Slab Energy

$E_{molecule}$: Molecule Energy

$E_{surface}$: Surface Energy

E_{bulk} : Bulk Energy

ΔA_{R-O} : Reduction Free Energy

λ : Reorganization Energy

1 INTRODUCTION

Hydrogen energy is the main energy source produced by processing and converting hydrogen gas into compounds found in nature and it is known for not harming the environment due to its rapid depletion (de Miranda, 2019). Hydrogen energy, known as the energy of the future, has been the subject of many studies because it is sustainable and environmentally preferable (J. A. Turner, 2004) . Hydrogen is the most abundant element in the nature, with the highest energy content compared to all conventional fuels. When used as fuel, the product release the atmosphere is only water or water vapor, so it is often preferred to be used as an energy carrier (J. Turner et al., 2008) . Hydrogen can be produced by many techniques, including biological and chemical such as water electrolysis (De Levie, 1999), steam and ethanol reforming (LeValley et al., 2014) , partial oxidation of hydrocarbons (Ashcroft et al., 1990), dark fermentation (Avcioglu et al., 2011), and photo-chemical water splitting (Junge et al., 2014) Hydrogen production from the electrolysis of water have been suggested by Rudolf Erren in the 1930s to be used as a fuel for transportation. In order to automotive emissions. However, water electrolysis needs external electric supply which also has a potential to cause CO_2 emission (Hoffmann, 2019). An alternative technique to the electrocatalytic method is the photo-chemical water splitting which this method can produce hydrogen by reducing water by absorbing photons in the visible spectrum. The advantage of this method is that it can convert sunlight into chemical energy by using direct solar radiation.

Photo-chemical water splitting process consist, of two main half reactions which are proton reduction and water oxidation. The process is known by converting two water molecules into an oxygen and two hydrogen molecules. Water splitting is a very complex reaction and therefore focusing into half-reactions, either water reduction or water oxidation is preferred. In this thesis we aim at investigating water reduction systems for photo-catalytic H_2 production using homogeneous and heterogeneous catalysts.

Homogeneous and heterogeneous catalysts preferred in photo-catalytic hydrogen production have their own advantages and disadvantages. In several studied systems, it has been observed that the transition metal Pt is used as the central atom in many proposed catalysts (Esswein & Nocera, 2007). However, it is inevitable that Pt metal, a catalytic reduction center, is not earth-abundant which hinders its large scale application. Instead, the photo-chemical water

splitting catalyst should contain inexpensive transition metals and result in high H2 production turnover frequencies (Losse et al., 2010) .

Significant progress has been made in the design of earth-abundant metal-supported molecular catalysts such as Fe, Ni, Co, which are used in many chemical reaction mechanisms (P. Wang et al., 2018). Among the catalysts reported for H_2 production, cobalt complexes with polypyridyl groups have received great attention due to their stability in aqueous solutions. The performances of cobalt-based catalysts with low over-potential and high frequency in hydrogen production have been already demonstrated. Several Co-centered catalysts containing Porphyrin, cobaloxime, pyrphyrin and polypyridine ligands, for instance, have been shown to be promising candidates for hydrogen evolution. Peter et al. investigated the catalytic activity of several cobalt complexes' having giglyoxime or propane bridged tetraimine ligands in acetonitrile. The results have showed that by using less electron-donating ligands, Co-complexes reduction could be readily and produce H_2. Compared with other ligand types, of polypyridyl ligands make strong ligand domain, high photocatalytic qualification and high stability provide superior to cobaloximes (Alberto et al., 2013) .

The major disadvantage in homogeneous catalysis, is the rapid recombination of electron and hole pairs (Kutal, 1983). In heterogeneous catalysis, on the other hand, the photocatalyst is combined with a supporting material, which prevents back electron transfer and stabilizes the reaction intermediates.

The photo-catalytic activity of Titanium dioxide (TiO_2), which is used in many industries such as dye, cosmetics and food, was discovered by Fujishima and Honda. Also, Goodeve and Kitchener showed the photo-catalytic performance of the TiO_2 surface, which can absorb UV light and generate oxygen, thus leading to photo-bleaching of dyes. This study also initiated several other studies to explore the photocatalytic reactions that can be catalyzed by TiO_2. This material has demonstrated success with its high stability, low cost, no side effects on humans and the environment, and ease of use on a large scale. Following, the effects of the photocatalytic activity of modified TiO_2, e.g. by cation-doping, on H_2 production has been investigated in the literature.

Regarding the mechanism of the H_2 production using heterogeneous catalysts, the water splitting first begins with the surface reaction of the photocatalyst. The photon is absorbed at or near the surface of the catalyst and various excitations occur depending on the energy of the incident photon. Ultraviolet and visible spectrum radiations excite valence electrons and cause photochemical reactions, as illustrated in Figure 1. When TiO_2 is excited with an energy

equal to or higher than its band gap, high energy electron moves to an electron conduction band (CB) from the valence band (VB) and creates a positive hole in the valence band. Due to this hole, the charge carriers can recombine among themselves. Metal or ametal co-catalysts are included in the system to prevent this recombination (Ipek & Uner, 2019).

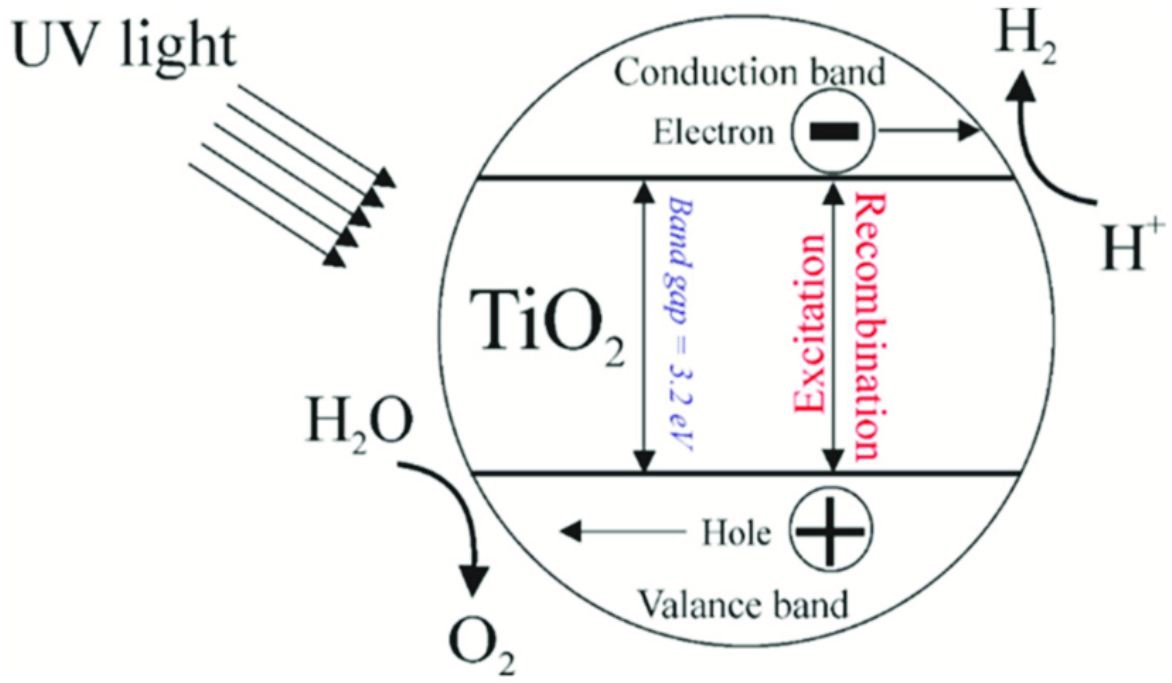

Figure 1: The mechanism of photocatalytic water splitting on TiO_2 based photocatalyst. Reprinted with the permission from Ref. (Anantharaj et al., 2016)

Titanium dioxide (TiO_2) is mostly used in research involving photocatalytic processes due to its absorption in the UV region (Su et al., 2012). The band gap energy (Eg) of TiO_2 is in the range of 3.0-3.2 eV, and it requires to absorb visible region radiation in order to increase the number of electrons in the conduction band(Dey et al., 2011) . However, less than 10 % of the sunlight is in the UV radiation zone. It has been demonstrated that the quality of TiO_2 to absorb sunlight is improved by various anion/cation (metal or ametal) dopants, which results in increased photocatalytic activity of the TiO_2.

It has been observed that Co^{2+} cation doped TiO_2 particles ,even in very small amounts, increase the photocatalytic activity of the overall system (Dvoranová et al., 2002). In addition to the doping with metals/ametals, adsorbing water splitting molecular catalysts on TiO_2

surface has become another solution for decreasing overall band gap and facilitating H_2 production. It was observed that continuous UV irridation of the unmetalated Pyrphyrin (Pyr) molecule adsorbed TiO_2 (110) surface causes decomposition of the Pyr molecule. However, metaled Pyr molecule with Co stabilizes the molecule against photo-reduced degradation (Graf et al., 2017). Besides, Co metalated Pyr molecule adsorbed on the TiO_2 (110) has shown to maintain its water reduction activity on the surface as in the homogeneous systems (Li et al., 2015).

TiO_2 is found in nature in three different phases: rutile, anatase and brookite. The most common are the rutile and anatase phases. Compared to the other phases, rutile phase is more stable at high temperatures. While the rutile and anatase phases are tetragonal, brookite has an orthorhombic structure. Differences of the lattice structure of TiO_2 also lead differences in electronic band structures. It is known that the rutile structure shows more photocatalytic activity than anatase (Reyes-Coronado et al., 2008). The electronic structure calculations of metal/ametal doped rutile and anatase surfaces have been modeled. In systems where atoms such as Iron, Aluminum , Silicon and Fluorine are doped, the anatase's phase stability is found to be higher than that of rutile with cationic doping support. However, the anionic doping of F adversely affects the stability (Hanaor et al., 2012). The adsorption and decomposition energies of water have been investigated using different surfaces of the rutile phase. The results show that the dissociative adsorption of water is more favorable on the 110 surface. However, the activation energy of water decomposition is greatest at the 100 surface (Zhao, 2014).

In this thesis, our aim is to investigate hydrogen production in homogeneous and heterogeneous systems by Ab-initio molecular dynamics and density functional theory. In the first part of the thesis, we study H_2 reaction mechanism of the Co-based planar catalyst immersed in aqueous solution. Following, we investigate adsorption of several Co-based molecular water splitting catalysts on the TiO_2 (110) surface with focusing on the adsorption geometry of the molecules as well as electronic structure rearrangements. Chapter 2 describes the addressed in this thesis, namely the experimental results of co-based catalysts modeled in homogeneous system and studies of several catalysts adsorbed on the TiO_2 surface. Chapter 3 reports all computational details and the fundamental theories of the computational methods. Chapters 4 and 5 discuss the hydrogen generation performance of the cobalt catalyst modeled in water and electronic structure analysis of the cobalt-centered molecular catalyst adsorbed on the TiO_2 surface, respectively.

2 LITERATURE REVIEW

2.1 Co-based Water Reduction Catalysts Solvated in Water

The H_2 generation performance of penta-pyridyl (CoaPPy) and tetra-pyridyl (CoaTPy) catalysts with different ligand structures were investigated by (Gurdal & Iannuzzi, 2020). They simulated all of the intermediate steps for the H_2 production mechanisms of the selected catalysts by applying Ab-initio molecular dynamics and density functional theory simulations. All the dynamic properties of the systems, solvent response and structural changes in the catalysts were monitored. According to the results, after the first electron transfer, the reaction continues with a singlet spin state. Experimental studies show that in the case of CoaTPy the cobalt center exhibits higher catalytic performance than CoaPPy (Alberto et al.,). Simulations reveal that CoaTPy interacts more with the surrounding water molecules during all intermediate steps which can be linked to the higher H_2 production performance measured experimentally. After the first reduction reaction, the reduction free energies for both CoaTPy and CoaTPy were calculated and the results show that while CoaTPy exhibits more negative reduction free energy for the first electron injection step, for the second reduction CoaPPy shows more negative reduction potential with 0.41 eV.

(Bachman and Alberto et al., 2013) investigated the H_2 production performances of pentadentate $CoPy_5$ and $Co(bPy)_2Py$ (Py: pridil and bPy: bi-pridil) and compared their results with the results obtained for tetradendate catalayst $Co(bPy)Py_2$ using Cyclic voltammogram and High Performance Liquid Chromatography. The $CoPy_5$ catalyst has a regular octahedral structure, excellent symmetrical coordination, and a penta-pyridyl ligand. The $Co(bPy)_2Py$ has two bi-pyridyl and one pyridyl groups and deviates from the ideal pentadentate coordination structure. As a result of the study, the Co(II/I) reduction potentials of the catalysts were measured as -1.3 V and -0.87 V for $CoPy_5$ and $Co(bPy)_2Py$, respectively.

(Queyriaux et al., 2018) investigated the hydrogen production performance of the new cobalt tetrapyridyl complex in aqueous solution. The solution contains a noble metal-free photosensitizer, water-soluble porphyrin, and ascorbate/tris-(2-carboxyethyl)phosphine (TCEP) sacrificial electron donor. The reaction occurs in an environment of pH 4.5. Considering the initial ECCE sequence, strongly acidic conditions are often required to protonate Co^{III}-H, a weaker nucleophile compared to Co^{II}-H. Therefore, the ECCE mechanism

is deterrmined to be improper under these conditions and reaction mechanism is suggested to be ECEC. The results prove that the catalyst under consideration has an active role in hydrogen production, producing 443 TONs – 3 mL of H_2 in aqueous solution.

(Guttentag, Rodenberg, Bachmann, et al., 2012) evaluated the Co(II/I) reduction potential of $Co(bPy)Py_2$ catalyst which contains one bi-pyridyl and two single pyridyl groups and deviates from the ideal pentadentate coordination. The Co(II/I) reduction potential of $Co(bPy)Py_2$ is measured as -1.11 V. Kinetic studies reveal that the H_2 production performances of $CoPy_5$, $Co(bPy)_2Py$, and $Co(bPy)Py_2$ catalysts were determined as 1200, 1400, and 9000 TONs (H_2/Co), respectively. Results showed that the number of pyridyl ligands, their sequence and structural geometry around Co metal have an effect on the catalytic activity. However, the reasons of the enhanced reactivity obtained for differently ligated catalysts have not been explained so far.

The hydrogen generating activities of the structures obtained with ortho, para and meta positions of the cobalt TPA complex (tris(2-pyridylmethyl)amine) which are depicted in Figure 2-(a) have been compared by (Guo et al., 2021).

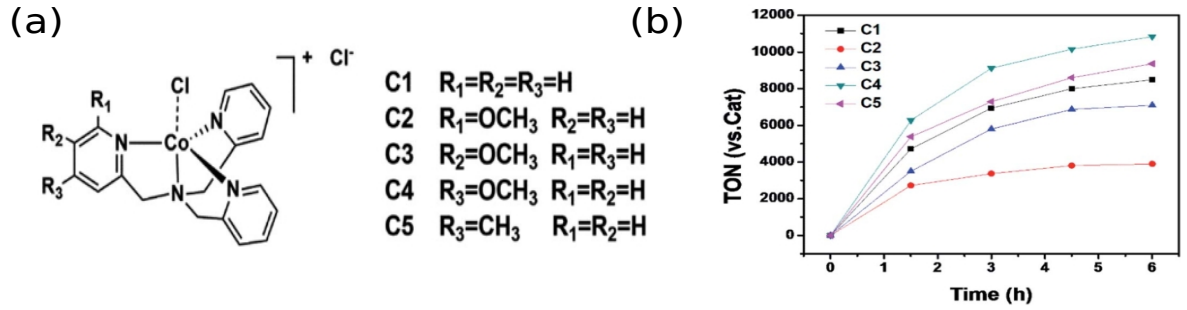

Figure 2: Structures of the examined cobalt complexes (a) and photocatalytic H_2 production profiles of the multi-component systems (b). For more details, see Ref. (Guo et al., 2021)

In the system characterized by UV-vis absorption spectroscopy, elemental analysis and cyclic voltammetry, good linear correlation has been obtained between Co–N bond lengths and Hammett constants of the substituents. Hammet constants affect the redox potentials of Co II/I and Co I/0 transitions as well as photocatalytic activities of the complexes. Structure C5 obtained by adding a methyl group to the cobalt complex has been used for comparison. All cobalt complexes have showed photocatalytic activity in the order of C4 > C5 > C1 > C3 > C2, see Figure 2-(b). Hammet constants have correlated closely with photocatalytic activity,

however the ortho-substituted C2 complex shows involvement of a steric effects during H_2 production (Guo et al., 2021) .

A study combining experiment and theory was conducted by (Rodenberg et al., 2015) for $Co(bPy)Py_2$ catalyst. Theoretical studies have shown that there are two spin states, singlet and triplet, for the Co(I) intermediate step modeled under vacuum. In the study, it was emphasized that it is possible that the H_2 cycle proceeds with the heterolytic ECEC mechanism and the possibility of the formation of Cobalt hydride, Co(III)-H, as a reaction intermediate step. However, they could not explain why the reaction proceeds with the singlet spin state although the triplet spin state of Co(I) has lower energy. They also could not explained why the first and second reduction potentials are measured higher and lower, respectively. In addition, Co spin density in other intermediates could not be determined experimentally and the heterolytic EECC mechanism was eliminated. (Guttentag, Rodenberg, Kopelent, et al., 2012) investigated the hydrogen production performance of cobalt-based catalyst in the presence of rhenium as a photosentezier in ascorbic and dehydroascorbic acid solution. When the solution is changed with pure water, results show that the hydrogen production performance in water is higher than the performance obtained in alkaline solution. Water reduction catalyst, $[Co^{III}Br_2\{(DO)(DOH)pn\}]$ and $[Re(CO)_3(py)(bipy)]^+$ the resulting system was able to produce hydrogen with significantly increased cycle numbers in the pH 2-6 range. Moreover, the reversibility of the Hasc–/DHA electron-donor/-acceptor pair was observed, providing acidic conditions to the system. During photocatalysis, oxidized ascorbate can be reduced again.

(Tong et al., 2014) showed that Co(tPy(bPy)Py catalyst with tri-pyridyl and bi-pyridyl ligands together with Ru-based photo-synthesizer has a TOF of 586 per hour at low catalyst concentration. However, the H_2 production mechanism or rate-determining steps have not been explained.(Leung et al., 2012) used the trans-$CoPy_4$ molecule as a water reduction catalyst having four pyridyl groups and a planar symmetry. It is shown that the catalyst has a performance of 1150 TONs H_2/Co. However, a mechanistic study examining the intermediate steps of the reaction could not be achieved.(Smolentsev et al., 2018) investigated the H_2 production mechanism of the $Co(bPy)_2Py$ catalyst by combining experiment and theory and investigated whether the single pyridyl group of the catalyst could be separated from the Co center following the first reduction reaction. Three structural models of the catalyst were modeled using DFT in a vacuum environment and the results were compared with the X-ray absorption near edge spectra (XANES). It was concluded from the study that the protons

could bond with the N atom in the pyridyl group leading to cleavage of the single pyridyl group from the Co center. Study suggests that the pyridyl group could be treated as a proton donor. (Joliat-Wick et al., 2018) investigated the H_2 generation performances of $Co(bPy)_2(CO)_2$ catalyst having two bi-pyridyl and one di-ketone groups in the planar structure. It has been shown that $Co(bPy)_2(CO)_2$ reaches a reaction rate of 60 nmol/s under optimum conditions, however the role of ketone groups or planar structure of the catalyst on reaction cycle has not been investigated.

Hydrogen generating activities of six different penta coordinated catalysts synthesized with N-methylbipyridine-2,11-diaza[3,3](2,6) pyridinophane as macrocyclic diazapyridinophan and cobalt complexes, see Figure 3-(a) have been investigated by photo-catalytic and electrocatalytic methods. When the performances of all complexes are compared, it is seen that the best result has been obtained using catalyst **4b** at pH 6 with 200 cycles (TON) while electrolytic H_2 production has been achieved with 140 TON at pH 7, see in Figure 3-(b). As a result performed DFT calculations, it has been demonstrated that the penta coordinated Co^{II}-H species are generally observed to be active in hydrogen production (P. Wang et al., 2019).

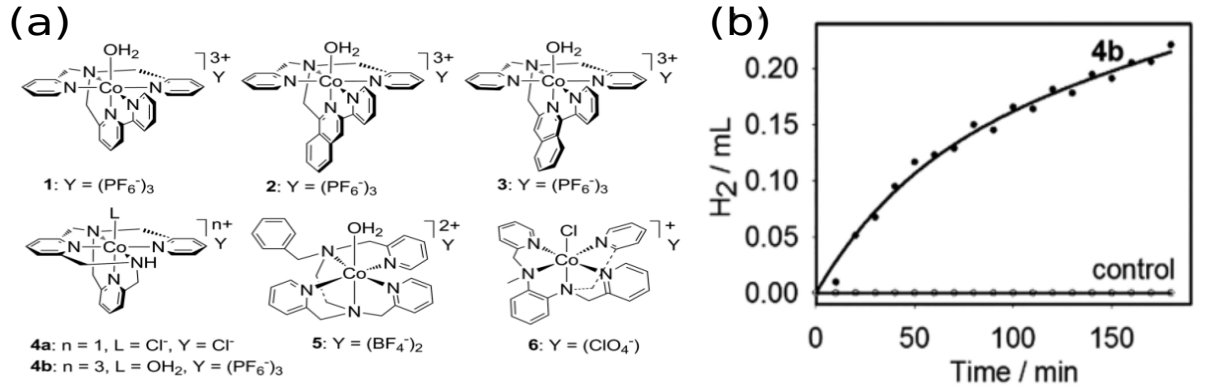

Figure 3: Mononuclear polypyridyl Co complexes (a) and H_2 generating activity with respect to the time for 4b catalyst. For more details, see Ref. (P. Wang et al., 2019)

(Sun et al., 2011) examined H_2 production performances of catalysts having Co reaction center and penta pyridyl groups as well as two methyl or trifluoromethyl groups in their structures. The study showed that the catalyst containing trifluoromethyl has a more positive Co(II)/Co(I) reduction potential. The protonation steps of the reaction have not been studied mechanistically.

(Schnidrig et al., 2017)experimentally investigated the H_2 generation performances of several poly-pyridyl catalysts including $Co(bPy)_2CO$. It has been shown that $Co(bPy)_2CO$ exhibits high stability during the reaction and it has a reaction rate of 20 nmol H_2/s under optimum conditions. It was concluded that the H_2 production reaction rate is increased by providing acidic conditions, implying the reaction mechanism is dependent on the amount of protons available in the environment. (Varma et al., 2013) examined the photo-catalytic H_2 production properties of four different water reduction catalysts in aqueous solution. In the systems, $[Ru(bpy)_3]Cl_2$ is used as a photo-synthesizer (PS), and four catalysts are selected as $[Co(CR)Cl_2]$ + cobalt(III) tetraaza-macrocyclic molecule (Cat1), $[Co\{(DO)(DOH)pn)\}Br_2]$ (Cat2), $[Co(dmbpy)_3]Cl_2$ (Cat3), and $[Rh(dmbpy)_2Cl_2]Cl$ (Cat4). Cat4 has shown the least H_2 generating activity. Cat2 and Cat3 have also shown promising results with respect to Cat1 and Cat4. Comparative investigations demonstrate that Cat1, despite being based on a non-noble metal, has a higher H_2 evolving activity in water than the bis-bipyridinyl rhodium complex $[Rh^{III}(dmbpy)_2Cl_2]^+$ (Cat4). As observed in acetonitrile solution, the greater catalytic performance of the PS/Cat1 system can be attributed to the strong stability of the low-valent Co^I oxidation state in the tetraaza-macrocyclic catalyst.

The reviewed literature is the current state of the art for photocatalytic H_2 production studies carried out using Co based Poly-pyridyl ligands. As noted, those studies lack mechanistic perspective of H_2 production reaction which is crucial for understanding rate determining steps and design catalysts accordingly. In the first part of the thesis we investigate planar $Co(bPy)_2CO$ catalyts in aqueous solution and we model the first and the second reduction steps using Ab-initio molecular dynamics, Density Functional Theory and Free Energy Perturbation Approaches.

2.2 Water Reduction Catalysts Adsorbed on TiO_2 Surface

The photo-catalytic activity of TiO_2 was first discovered by (Fujishima & Honda, 1972), which further increased the use of this material. Also, (Goodeve & Kitchener, 1938) showed the TiO_2 surface photocatalytic activity, that can absorb UV light and generate oxygen, thus leading to photo-bleaching of dyes. This work was also the first step of many researchers to explore the photocatalytic reactions that can be catalyzed by TiO_2. For instance, the effects of the photocatalic activity of cation doped TiO_2 on H_2 production has been investigated (Dvoranová et al., 2002). It has been observed that transition metals added to TiO_2 particles,

even very small amounts, can increase the photocatalytic property of the catalyst by decreasing the band gap (Dvoranová et al., 2002).

(Nikolaidis & Poullikkas, 2017) investigated the adsorption of Au, Ag and Cu transition metals on TiO_2 (110) rutile surface applying DFT simulations. For the adsorption of Au on the rutile surface, it was found that the most favorable surface sites for Au are the O(3c), Ti(5c) and bridge O(2c) atoms, where 2c (3c or 5c) abbreviation refers to "two-coordinated". The Au adsorption energy on the surface is calculated as ≈0.6 eV. According to the results, adsorbed Au has a covalent interaction with Ti(5c) and an ionic interaction with O(2c). Ag and Cu atoms establish bond with the bridge position between surface O(2c) atoms. Adsorption energies are computed as 1.01 eV and 1.80 eV for Ag and Cu, respectively. In contrast to Au, Ag and Cu have a substantially weaker contact with a vacancy site than the stoichiometric surface. When a metal atom is placed on a vacancy site, some charge from the defect is transferred to the metal, forming a strong ionic metal-defect bond. The transferred charge is likely to fill the anti-bonding states of Ag and Cu and hence disrupt the Cu or Ag adsorption for Cu or Ag (with a singly occupied outer s orbital). Charge density difference maps show that covalent interaction with Ti(5c) d orbitals primarily responsible for the Ag and Cu bonding to the surface.

By using the Ab-initio approach, (Y. Wang & Hwang, 2003) et al., studied the adsorption of the Au atom on the TiO_2 rutile 110 surface. Covalent and ionic bonding interactions with the 5 coordinated surface Ti_{5c} and bridging O atoms, respectively, are worked in concert to support Au adsorption in the H_2 region (fourfold hollow over the in-plane O(3c), the Ti(5c) and the bridging O(2c)). There is a very strong ionic connection between Au and the nearby 6 coordinated Ti_{6c} atoms that facilitates Au adsorption on the decreased surface. The proximity of oxygen vacancies in the [0 0 1] direction has a considerable impact on the Au adsorption energy in the defect region. For the Au atom, the H_2 region (four-fold hollow over the in plane O_{3c}, Ti_{5c} and O_{2c} bridge) has been found to be the most stable adsorption site. DFT GGA results unequivocally has been demonstrated that an oxygen defect region has a much greater affinity for Au with respect to the stoichiometric surface.

In one another study, Ni atom is adsorbed on the 001 anatase surface of titanium dioxide with singlet, triplet and quintuple spin states. The DFT method is used to calculate the energy of the atom adsorbed on different parts of the surface. Different adsorption sites have been discovered in the surface defects. For the triple multiplicity case, two deep minimums with adsorption energies of 3.5 and 3.74 eV have been discovered at 0.55 and 0.11 Å from the

surface of the bridging oxygen plane. At relaxed plate surfaces, both of these minima show spin transfer from Ni to Ti atoms. As a result of the calculations, it has been determined that the spin multiplicity of the system is singlet for high coverages (Escamilla-Roa et al., 2012).

DFT exploration of Co-based water reduction catalyst, CoPyr, adsorbed on the TiO_2 (110) surface has revealed the decreased band gap of the system which opens the doors for the photocatalytic H_2 production (Gurdal et al., 2015). It was observed that the interactions between cyano groups of the molecule and the Ti centers of the surface has an effect on stabilizing the molecule on the different surface region (see Figure 4). With this interaction, re-hybridization of the molecular orbitals localized on the cyano groups is achieved.

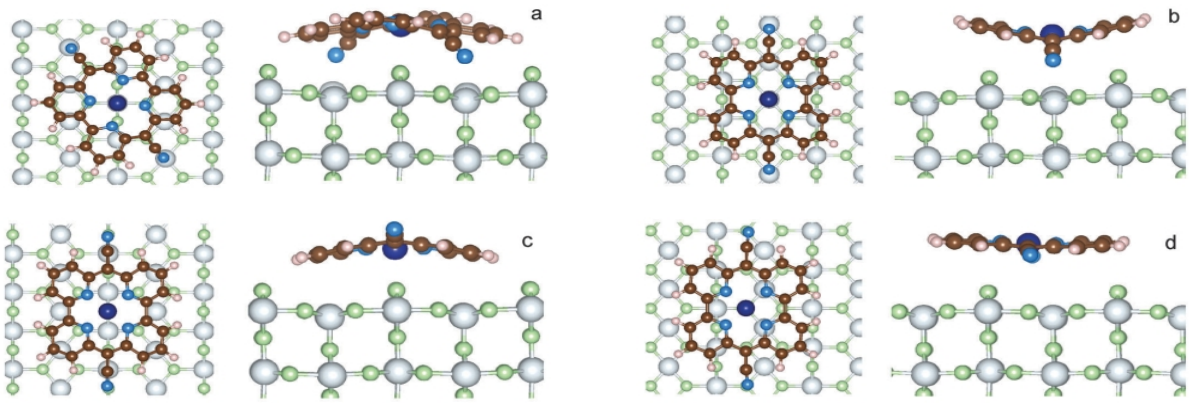

Figure 4: The CoPy@rutile complex has four different optimal structures that were created from different molecule-initial positions. For more details, see Ref. (Gurdal et al., 2015)

Thus, the lowest unoccupied molecular states are realigned. Adsorption of CoPyr catalyst on the TiO_2 rutile surface provides a significant decrease in the energy gap of the system (from 3.2 eV to 1.5 eV) compared to the pristine rutile(110). Thus, when visible light is absorbed, direct or indirect electrons' injection from CoPyr to the rutile (110) surface is, in principle, allowed. Adsorption, on the other hand, has no effect on the electrical characteristics of the Co(II) center, indicating that CoPyr and its derivatives can be employed in water reduction for hydrogen production also in the adsorbed state.

Adsorption of Co to four different regions of the TiO_2 anatase surface has been investigated by (Zuo et al., 2009) by applying the DFT/local density approximation (LDA) method. Adsorption is characterized as chemical adsorption on the anatase surface. According to the density of states (DOS) analysis, the highest occupied molecular orbital (HOMO) has been

mostly filled by Co 3d orbitals. The results showed that there is significant hybridization between O 2p and Co 3d orbitals in the valence regions of the substitution sites.

It has been shown that Cobalt doping on a single-crystal TiO_2 rutile surface enhances photo-absorption properties of the system (Zuo et al., 2009). Co doping also results in the formation of nanostructures and anisotropic ripple sites. It was observed that the functionalized surfaces increase the photon absorption rate in the UV and visible regions by approximately two and and five times, respectively. The improved photo-absorption reported in this study is attributed to the formation of nanostructures, generation of oxygen vacancies, and Co-ion associated ligand field changes. The nanostructured TiO_2 surfaces explored in this study, indeed, offer a wide range of photocatalytic applications (Yang et al., 2007).

(Graf et al., 2017) experimentally and theoretically investigate adsorption and metalation of tetradentate bipyridine-based macrocycle pyrphyrin (Pyr) on stoichiometric TiO_2 (110) surface. The methods performed in this study include scanning tunneling microscopy (STM), photoelectron spectroscopy, low energy electron diffraction and density functional theory. When the CoPyr/TiO_2 system is excited by light, the energy level alignment of the CoPyr/TiO_2 promotes electron injection into TiO_2. The optimal adsorption geometry obtained by DFT simulations, in which the molecules support convex bridging oxygen sequences, is consistent with low coverage adsorbed Pyr molecules' STM images. Molecular states within the substrate band gap for Pyr and CoPyr are discovered with relatively minor energy shifts during metalation, which agrees with the DFT estimates. Continuous UV-irradiation causes rapid decomposition of Pyr molecules, but Co-incorporation stabilizes the molecules against photo induced degradation. This result improves that CoPyr stability is critical for the possible use of TiO_2 in dye sensitization.

In the second part of the thesis, cobalt-based water reduction catalysts having planar structures previously synthesized and tested for homogeneous H_2 production have been investigated by means of DFT. The adsorption geometries of the catalysts on the rutile(110) surface have been determined and further electronic density difference analysis has been performed for a selected catalyst/TiO_2 complex.

3 MATERIALS AND METHODS

In this thesis, the hydrogen evolution activity of cobalt-based catalysts is modeled by density functional theory and Ab-initio molecular dynamics simulations in both homogeneous and heterogeneous environment. In this section, the basis of density functional theory and Ab-initio molecular dynamics simulations used in all electronic structure calculations are summarized.

3.1 Density Functional Theory and Ab Initio Molecular Dynamics

Density Functional Theory (DFT) is a technique that has acquired a lot of attraction and has become one of the most extensively used tool for calculating electronic structures of systems. It has several advantages over Hartree–Fock techniques, including it requires less computational effort and in some circumstances (especially for d-metal complexes) gives better agreement with experimental results (Atkins et al., 2014). DFT is based on electron density as contrarily to electronic wave function. Kohn-Sham equations are formed by expressing the Schrodinger equation in terms of electron density (ρ). Hohenberg, (Kohn & Sham, 1965) introduced DFT in 1964 as a ground-state energy minimization problem. The method entails transferring any fully interacting problem to a non-interacting problem using exchange–correlation functionals, as shown in Equation 3.1.

$$E = E_{XC}[\rho(r)] + T_s[\rho(r)] + J[\rho(r)] + \int \upsilon_{ext}(r)\rho(r)dr \tag{3.1}$$

$E_{xc}[\rho(r)]$ term represents the contribution of exchange-correlation energy. $T_s[\rho(r)]$ is the non-interacting system's kinetic energy. The classical Coulomb repulsion energy is $J[\rho(r)]$, while the interaction of the external potential acting on the electrons is $\int \nu_{ext}(r)\rho(r)dr$. All of these concepts are referred to as functionals, and they are dependent on the electron density (ρ), i.e. the number of electrons per unit volume. Chemical/biological systems have millions of electrons which interact with each other. As formulated by the Kohn-sham equation, electronic energy includes kinetic energy of the single electron, the kinetic energy due to the interaction of many electrons in the many body system, the repulsion term of the single

electron, repulsion term of many body system, and electron-nucleus attractions (Koch & Holthausen, 2015).

Calculation of single electron terms is straight-forward by applying the known formulations of kinetic energy and coulomb interactions. However, the interactions counting many body systems do not have a mathematical function and all these terms are included in the exchange-correlation energy functional. Various theories have been put forward for formulating this functional and granting the energy raised due to the many body interactions. The proposed equations for the exchange-correlation energy functional and the calculated properties of the systems are compared with the corresponding experimental results which give hint if the proposed functional well describes the system under consideration or not. If the experimental results are not well predicted, then the formulation of the proposed exchange-correlation energy functional is modified or changed. For the exchange-correlation term, as shown in Equation 3.2, correlation is a term that arises due to the interaction of electrons with each other (Koch & Holthausen, 2015). The term exchange derives from the fact that electrons can be filled differently in vacant orbitals and the system tries to find the most stable configuration among spin up or spin down configurations. Therefore, both orbital and up-down spin state of electrons change.

$$E_{xc}[\rho(r)]=(V_{ee}[\rho(r)]-J[\rho(r)])+(T[\rho(r)]-T_s[\rho(r)]) \tag{3.2}$$

where T [ρ(r)] is the kinetic energy of the interacting system and V_{ee}[ρ(r)] is the non- classical interaction between electrons.

In a nutshell, in DFT, first the electron density is estimated. A superposition of atomic electron densities is used for this step. Then, Kohn-Sham equations are used to obtain an initial orbital set. This set of orbitals are then iterated to reach the closest result of the electron density estimated in the first step. Therefore, the process continues until the energy and density are constant within a tolerance (Atkins et al., 2014).

Ab-initio Molecular Dynamics (AIMD) combines electronic structure calculations with the sampling of the phase space, thus makes it possible to study the configurational rearrangements under realistic experimental conditions. It is a widely applied method for studying reaction mechanisms (Guidon et al., 2008). In the AIMD method, exploration of

conformational space takes place at finite temperature with the generation of trajectories of a several picoseconds. The numerical integration of the equations of motion enables the generation of phase-space trajectories (Hanaor et al., 2012). The Born-Oppenheimer approximation is used in all molecular structure theories. Since nuclei are so much heavier than electrons, it is assumed that they move relatively slowly and can be viewed as stationary while electrons flow around them. Therefore, we can decouple movements of nuclei and electrons and assume that the nuclei is kept fixed. Following this assumption, Schrodinger equation can be performed for calculating electronic energy (Barnett & Landman, 1993).

At each time step along the AIMD trajectory, energy and forces are calculated on the fly. This obviously necessitates enormous computer resources, much above those required for single point calculations or even geometry optimizations, for a moderately lengthy sampling of the phase space. Empirical or semi-empirical models could be used to reduce computational expenses.

One of then drawback of the AIMD is that rare events cannot be simulated within reasonable processing time frames, adequate sampling of the phase space, which may include several energetically deep and separated wells. Many techniques have been proposed to improve phase space exploration. Metadynamics (MTD) (Laio & Parrinello, 2002) is one of these approaches, which uses a history-dependent bias potential to sample the free energy surface (FES) uniformly. The method allows the capture of rare events by encouraging the trajectory to visit previously unexplored regions of phase space. Collective variables (CV) selected in the system are used to define the dimension of the free energy surface (FES). Hence, several rare events can be captured (Barducci et al., 2011).

3.2 Computational Methodology

3.2.1 Co-based Water Reduction Catalyst Solvated in Water

The CP2K/QUICKSTEP package is used for the electronic structure calculations. The CP2K program is an open source program and is written in Fortran 2003 language. It uses libint, fftw3, libxc, elpa, scalapack libraries along with MPI and CUDA multi-threading. Electronic structure calculations are performed at Kohn-Sham DFT level using Gaussian and plane wave (GPW) formalism (VandeVondele et al., 2005). While CP2K includes the Khon-Sham formalism, it can use Gaussian and Plane Wave approaches together by performing Fast

Fourier Transforms, which makes calculations faster compared to many simulation packages. Valence electrons are explicitly described, and the interactions between the valence electrons and the atomic cores are described using norm-conserving Goedecker–Teter–Hutter (GTH) pseudo potentials (Goedecker et al., 1996). For Co, O, C, H, and N, the valence shells contain 17, 6, 4, 1, and 5 electrons, respectively. For all atomic types, double-zeta valence plus polarization (DZVP) basis sets optimized on molecular geometries (Mol-Opt technique) are used (VandeVondele & Hutter, 2007). The auxiliary plane wave basis set has a cutoff of 400 Ry. Spin polarizations and periodic boundary conditions are always used. We perform AIMD simulations in order to model initial state of the system as well as the intermediate steps. In order to relax the catalyst/water system as well as determine the simulations box volume, (AIMD) simulations in isobaric-isothermal (NPT) ensemble have been carried out for approximately 20 ps. Integration time step is set to 0.5 fs. The cubic simulation volume of $Co(bPy)_2CO$/water system is determined as 6012.95 $Å^3$ where AIMD/NPT systems contain 215 water molecules. Following, AIMD simulations in canonical (NVT) ensemble have been carried out in order to model initial state of the system as well as an intermediate step. The canonical sampling through velocity rescaling (CSVR) (Bussi et al., 2007) thermostat with a time constant of 100 fs is applied in order to keep simulation temperature constant at 300 K.

In our study, initial state and the first reduction step are modeled using AIMD simulations (VandeVondele & Hutter, 2007). Perdew-Burke Ernzerhof's (PBE) general gradient approximation (GGA) is used as the exchange-correlation functional (Perdew et al., 1996) in AIMD simulations. Van der Waals (vdW) interactions are computed self-consistently using the Vydrov-Voorhis (rVV-10) van der Waals density functional (Sabatini et al., 2013).The empirical short-range interaction parameter of the rVV-10 density functional is set to 9.3 (Ambrosio et al., 2015) . The auxiliary density matrix method (ADMM) that ensure an important speeding is used for all hybrid functional calculations (Guidon et al., 2010). The electronic properties of the catalyst following the first electron injection is monitored by distribution of the frontier orbitals, namely the highest occupied (HOMO) and the lowest unoccupied (LUMO) molecular orbitals. Molecular orbital distributions have been calculated using PBE0-rVV10 density functional.

Co-based Planar Tetra-pyridyl Catalyst in Vacuum

Figure 5-(a) illustrates the ball and stick sketches of the $Co(bPy)_2CO$ catalyst. $Co(bPy)_2CO$, which shows planar symmetry, has two bipyridyl ligands link to each other by a ketone group. The four pyridine rings are attached to the central cobalt atom by four N atoms. Figure 5-(b) shows the two closest water molecules coordinated with the cobalt center. Since the catalyst has a planar structure, the water oxygens in front of and behind of the catalyst interact directly with the cobalt. The catalyst in solvated in 215 water molecules in order to mimic the solvent environment around the catalyst, see Figure 5-(c).

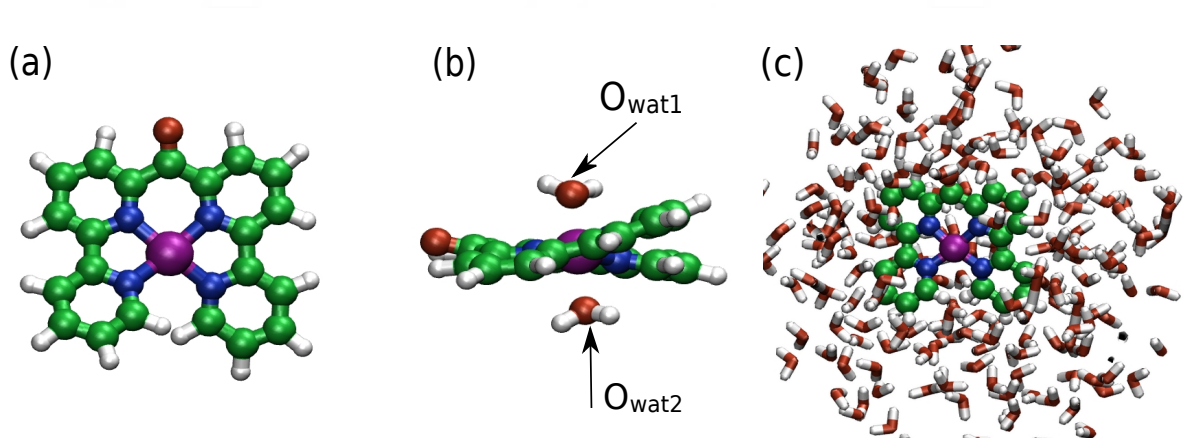

Figure 5: Ball and stick representations of a) $Co(bPy)_2CO$, b) Two water molecules which are closest to the Co center. The oxygen belonging to the first closest water molecule is labeled as O_{water1} , while the solvent's second-closest oxygen is shown with O_{water2} . c) Catalyst solvated in 215 water molecules. Color code: green: C, white: H, purple: Co, blue: N, red: O.

Catalytic Cycle for H_2 Production

Concerning the H_2 production reaction mechanism which including 4 reaction intermediate steps, 2 reductions and 2 protonations in total. Depending on the sequence of reduction and protonation reactions, H_2 production mechanism differs. Here, we investigate subsequent electron injections followed by protonations mechanism which is abbreviated as EECC. E and C stand for electron transfer and protonation step, respectively.

The fundamental catalytic state is $^{2}(Catalyst)^{+2}$ and the first electron injection to this initial state might result in one among two possible states with different multiplicities, triplet $^{3}(Catalyst)^{+1}$ or singlet $^{1}(Catalyst)^{+1}$. Both spin states are modeled using AIMD simulations in order to determine the spin state of the first protonation reaction, since depending on the spin state of the first electron injection, the next intermediate step, first protonation, can give triplet or singlet state $Co(bPy)_2CO$-H species. Following the second reduction and second protonation the reaction cycle is completed, H_2 should be, in principle, produced and the system should yield back $^{2}(Catalyst)^{+2}$ with the spontaneous release of H_2 .

Figure 6 shows the EECC mechanism for the $Co(bPy_2)CO$ catalyst consists of reduction and protonation steps. In the notation as $^{3}(Catalyst)^{+1}$, 3 represents the spin multiplicity of the system and +1 represents the charge of the system. After the second electron injection, the system continues to the next step with a doublet spin multiplicity. Following the protonation step, the spin multiplicity of the system becomes doublet or quartet. Following the second protonation, the H_2 production reaction cycle is completed.

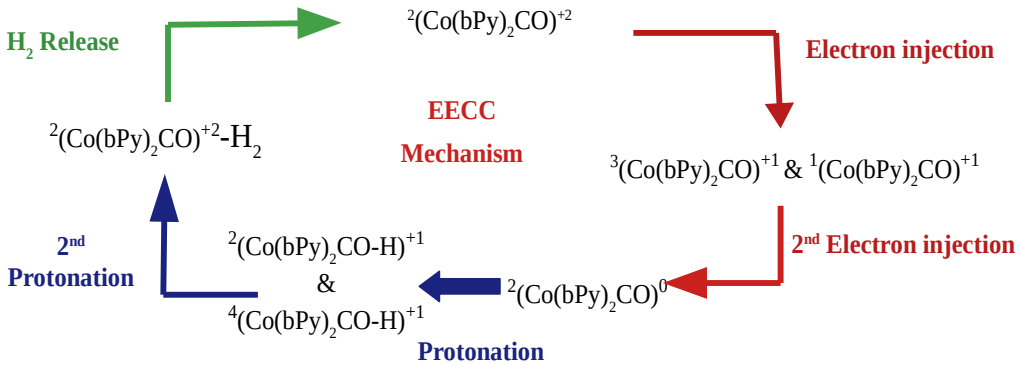

Figure 6: Demonstration of EECC mechanisms for hydrogen production by $Co(bPy)_2CO$ catalyst. Figure illustrates all the intermediate steps for the H_2 production. The nomenclature $^{m}(Catalyst)^{+q}$ refers to the total charge +q and the multiplicity m. E and C stand for electron transfer and protonation step, respectively.

3.2.2 Calculation of the Redox Potentials

The procedure for calculating the redox potential for an electron injection step is summarized in this section. The reduction reactions of interest are of the type

$$\text{First } e^- \text{ injection} : {}^{2}(Co(bPy)_2CO)^{2} + e^- \rightarrow {}^{1}(Co(bPy)_2CO)^{1}$$

$$\text{Second } e^- \text{ injection} : {}^{1}(Co(bPy)_2CO)^{1} + e^- \rightarrow {}^{2}(Co(bPy)_2CO)^{0}$$

These are half reactions, with n electrons in the oxidized state O and n + 1 in the reduced state R. The ratio of the respective partition functions, which can be rewritten as the ensemble average over the exponential of the vertical energy difference $\Delta E_0(R^N) = E_R(R^N) - E_O(R^N)$, gives the free energy difference between the R and O states, where R^N represents the instantaneous configuration of N particles. Using vertical energy gaps, reduction free energy is calculated using the following formulation:

$$\Delta A_{R-O} = -k_B T \left[\ln \langle \exp(-\beta \Delta E) \rangle_R + \ln \langle \exp(-\beta \Delta E) \rangle_O \right] \qquad (3.3)$$

In here, $<...>_M$, gives the ensemble average obtained by AIMD trajectory for system having state M. If the electron transfer obeys the Marcus Theory, then Equation 3.3 is simplified to Equation 3.4 using lineer solvent response assumption (Marcus, 1956).

$$\Delta A_{R-O} = \frac{1}{2}[\langle \Delta E \rangle]_R + [\langle \Delta E \rangle]_O \tag{3.4}$$

In this case, $\langle \Delta E \rangle_R$ and $\langle \Delta E \rangle_O$ where R (reduced) and O (oxidized) respectively gives the ensemble average of the vertical energy gap between R-O and O-R transitions. The important assumption here is that the electron movement is much faster than the atomic nucleus movement, so when the system is transferred from O to R state by having electrons, the same atomic core coordinations are preserved for O and R states and the number of electrons is increased by +1 only in the R system. The ensemble average $\langle \Delta E \rangle_R$ can be calculated by taking ensemble average of the energy differences between selected O and R snapshots obtained using AIMD trajectories. As the same vein, $\langle \Delta E \rangle_O$ can be calculated by taking ensemble average of the energy differences between selected R and O snapshots.

Furthermore, the solvent response can be defined by a quantity known as reorganization free energy, which is calculated as the difference between the mean energy gaps, see Equation 3.5.

$$\lambda = \frac{1}{2}[\langle \Delta E \rangle]_R - [\langle \Delta E \rangle]_O \tag{3.5}$$

3.2.3 Adsorption of Co-based catalyst on TiO_2 Surface

The rutile (110) lattice has tetragonal space group of $P4_2$ /mnm (No. 136) (Howard et al., 1991). On the rutile surface, all of Titanium atom is bonded by six O atoms. O atoms are coordinated with three-fold by Ti. Our slab model consists of 5 layers and a total of 162 atoms. Periodically repeated layers are optimized under a vacuum of 20 Å. Thus, the interaction between the surfaces are prevented. While calculating the adsorption energy of the system and geometry optimization simulations the bottom 3 layers are kept constant. The surface interactions of the catalyst are provided by the upper 2 layers.

Geometry optimizations are started by locating cobalt-based water reduction catalyst at a distance of 5 Å above the rutile surface. The adsorption energy of the system is calculated as shown in Equation 3.6.

$$E_{adsorption} = E_{compleks} - \left(E_{slab} + E_{molecule}\right) \tag{3.6}$$

$E_{complex}$ refers to the energy of the system in which the molecule and the surface are included. E_{slab} is the energy of the only surface, $E_{molecule}$ is the energy of the catalyst.

The CP2K/QUICKSTEP package is used for the electronic structure calculations. Electronic structure calculations are performed at Kohn-Sham DFT level using Gaussian and plane wave (GPW) formalism (VandeVondele et al., 2005). Valence electrons are expressly described, and the interactions between the valence electrons and the atomic cores are described using norm-conserving Goedecker–Teter–Hutter (GTH) pseudo potentials (Goedecker et al., 1996). The valence shells contain 12, 6, 17, 4, 1, and 5 electrons for Ti, O, Co, C, H, and N, respectively. For all atomic types, double-zeta valence plus polarization (DZVP) basis sets optimized on molecular geometries (Mol-Opt technique) are used (VandeVondele & Hutter, 2007). The auxiliary plane wave basis set has a cutoff of 600 Ry. Spin polarizations and periodic boundary conditions are always used. Perdew-Burke Ernzerhof's (PBE) general gradient approximation (GGA) is used as the change-correlation functional. The auxiliary density matrix method (ADMM) that ensure an important speeding is used for all hybrid functional calculations (Guidon et al., 2010). The Grimme-D3 scheme is applied to the dispersion interactions according to for the optimization of the geometries.

Cobalt Based Catalysts and Rutile Surface

The hydrogen production performance of catalysts under consideration have been previously synthesized and their water reduction performances have been characterized in previous experimental studies. Ball and stick representation of the catalysts are shown in Figure 7. Catalysts with planar structure are named as (a) Co-bipyrydine ($Co(bPy)_2CO$) **Cat1** (Schnidrig et al., 2017) (b) Co-diketo Pyrphyrin **Cat2** (Joliat-Wick et al., 2018) (c) Cobalt tetraaza-macrocyclic ($[Co^{III}(CR)Cl_2]^+$) **Cat3** (Varma et al., 2013) and (d) Cobalt tetrapyridyl complex **Cat4** (Queyriaux et al., 2018). The pyridine rings of the catalysts consisting of four pyridine rings are attached to the cobalt center with the N atom. Unlike the others, only Co(bPy)CO and Co diketo Pyrphyrin have pyridine rings linked by O atom. Co diketo-Pyr

catalyst contains a diketo group by bonding with two O atoms. The **Cat4** catalyst consists of a single pyridine ring.

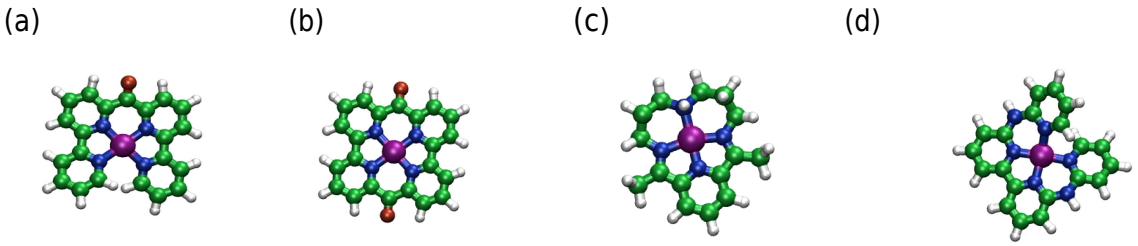

Figure 7: Ball and stick representations of (a) $Co(bPy)_2CO$ (Cat1), (b) Cobalt diketo-Pyrphyrin (Cat2) , (c) $[Co^{III}(CR)Cl_2]^+$ (Cat3) and (d) cobalt tetrapyridyl complex (Cat4). Color code: green: C, white: H, purple: Co, blue: N, red: O

The most stable surface of rutile is (110), and it is commonly employed in engineering applications. To model such a surface, a symmetrical planes of several atomic layers is cut along the (110) surface without stack splitting. A adequately large vacuum distance (20 Å) is added to the surface in order to avoid interference with periodic images in the vertical direction. As depicted in Figure 8, the surface unit cell consists of two Ti and four O atoms. Two of the Ti atoms located in the same plane. O atoms are in the same plane with Ti, one above (sticking out O) and one below. One Ti atom of surface has six bonds (Ti_{6c}), the second Ti atom is coordinated with five-fold (Ti_{5c}). The O atoms of surface, on the other hand, are three coordinated (O_{3c}), or two coordinated (O_{2c}). The TiO_2 slab is modeled using 5 atomic layers where top two layers are relaxed during the simulations in order to mimic surface of the material. While bottom 3 layers are always kept fixed at bulk coordinates.

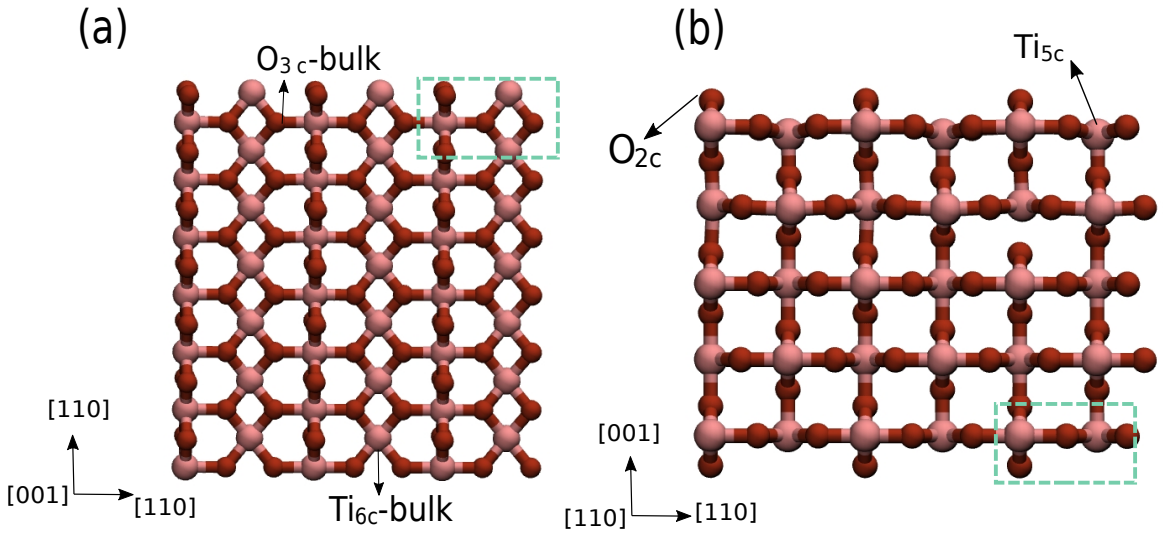

Figure 8: Ball and stick sketches of the rutile (110) slab, where layers' number is set to 5. (a) Side perspective of the surface and (b) top perspective of the surface. O_{2c} , O_{3c} , and Ti_{5c} are shown as surface atoms, $O_{3c\text{-}bulk}$ and $Ti_{6c\text{-}bulk}$ are shown as bulk atoms. The dashed green box indicates the surface unit cell. Color code: pink: Ti, red: O.

4 RESULTS AND DISCUSSIONS

4.1 Co-based Water Reduction Catalyst Immersed in Water

We first optimize the geometry of the catalyst in vacuum by applying DFT and PBE/rVV10 density functional. At the initial state of the catalyst, the spin multiplicity of the $Co(bPy)_2CO$ molecule is determined as doublet and the total charge of the system is +2. Figure 9 shows the optimized geometry of the Co-based planar catalyst having two bipyridine ligands around the Co reaction center. The optimized distances between the Co center and the surrounding N atoms are reported in the Table 1. The catalyst maintains its planar structure after the optimization carried out under vacuum. The Co-N distances are measured around 1.90 Å.

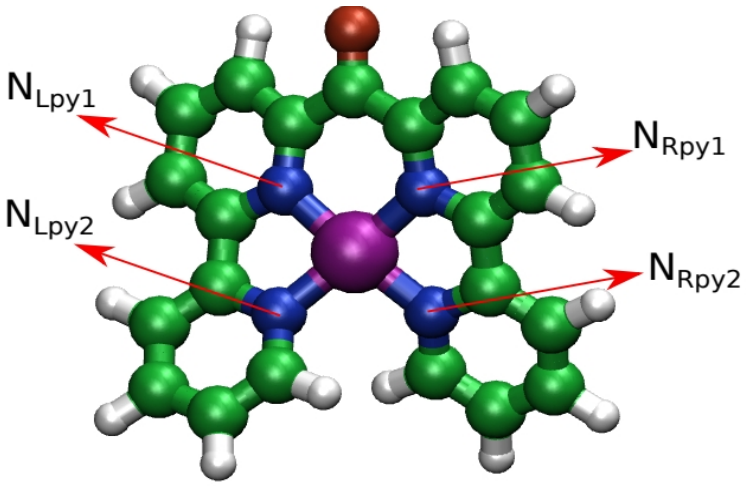

Figure 9: Co-based molecular catalyst $Co(bPy)_2CO$ under consideration. Color code: green: C, white: H, purple: Co, red: O, blue: N. Among the Ns in the bipyridine ligands around the Co atom, those on the right hand side are labeled as N_{Rpy1}, N_{Rpy2}, and those on the left hand side are labeled as N_{Lpy1}, N_{Lpy2}.

Table 1: The distances between the central Co and N atoms of the catalyst which is optimized under vacuum.

Distances (Å)	
Atom pair	$Co(bPy)_2CO$
$Co\text{-}N_{Rpy1}$	1.90
$Co\text{-}N_{Rpy2}$	1.92
$Co\text{-}N_{Lpy1}$	1.90
$Co\text{-}N_{Lpy2}$	1.92

Following optimization of the catalyst under vacuum, it is dissolved in 215 water molecules (explicit solvent) using Visual Molecular Dynamics (VMD) ((Humphrey et al., 1996) in order to model catalyst/water system and intermediate steps of the water reduction reaction. The volume of catalyst-water simulation box is relaxed by carrying out Ab-initio molecular dynamics (AIMD) simulations at the isobaric-isothermal (NPT) ensemble for approximately 20 ps. In the simulations, the atomic number is kept constant at ≈ 700, the pressure at 1 atm, the temperature at 300 K. Simulation temperature and potential energy calculated during AIMD-NPT simulations are depicted. Simulation results show that we have small fluctuations around 300 K for temperature and the potential energy of the system is preserved after about 10 ps simulation time. The cubic simulation volume for $Co(bPy)_2CO$ shows small fluctuations at 6012.95 $Å^3$. Therefore, one side length of our $Co(bPy)_2CO$/water cubic simulation box is determined as 18.18 Å.

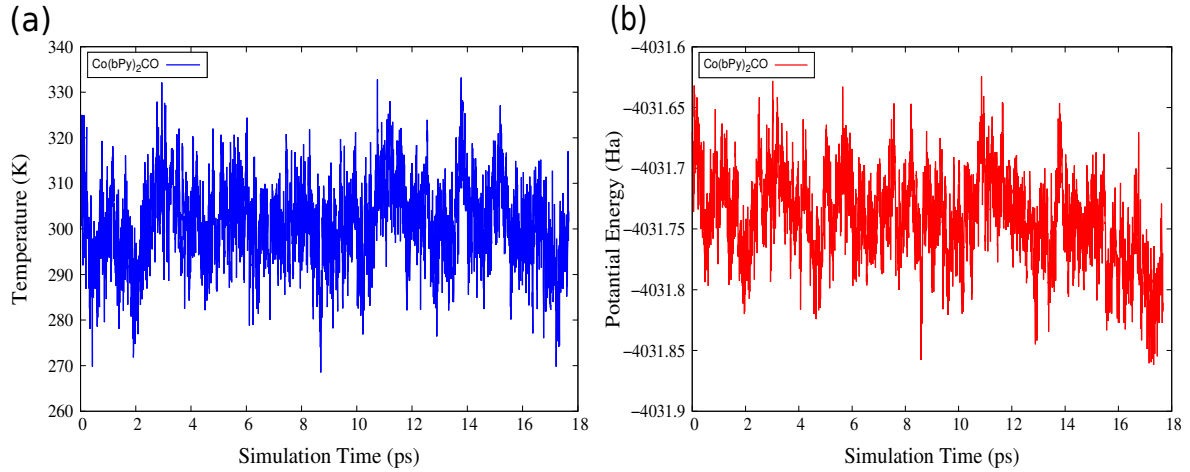

Figure 10: AIMD-NVT simulation results for the initial step of the H_2 generation mechanism continued at approximately 20 ps. (a) Temperature change and (b) potential energy change with respect to simulation time.

In the initial state of the EECC mechanism, the spin state of the $Co(bPy)_2CO$ catalyst is determined as 2 and the total charge of the system is +2. Following the determination of the simulation volume by NPT ensemble simulations, we model the initial state of the catalyst/water system applying NVT ensemble also known as canonical ensemble which is carried out at constant number of molecules, constant volume and constant temperature conditions. AIMD-NVT simulations of the catalyst modeled in water are completed at approximately 20 ps. The potential energy and temperature changes of the system during the AIMD-NVT simulation are shown in Figure 10 with respect to the simulation time. According to the Figure 10, we observe small fluctuations for simulation temperature and potential energy.

The snapshots for the initial state of the catalyst $^2(Co(bPy)_2CO)^{+2}$ acquired at 17.67 ps are shown in Figure 11 (a) and (b). Two water molecules, one in the front and the other in the back of the catalyst, are in direct coordination with the Co center. The oxygen atoms of these closely coordinated water molecules are labeled as O_{wat1} and O_{wat2}, respectively. These water

molecules are very structured around the Co and the distance between Co and O_{wat1} (O_{wat2}) fluctuates around 2.25 Å during the simulation, as depicted in Figure 11-(c).

In fact, the coordination between Co and O_{wat1} (O_{wat2}) is so strong that during the simulations no conformational changes in these water molecules have been observed. The distances between N atoms of the planar bipyridine ligands and the Co atom are plotted in Figure 11-(d). The atomic distances between each Co-N are very similar to each other and fluctuate around 1.9 Å during the simulation. Separation of the bipyridine ligands from the Co center have not been observed, thus the catalyst maintains its stable structure in water solvent.

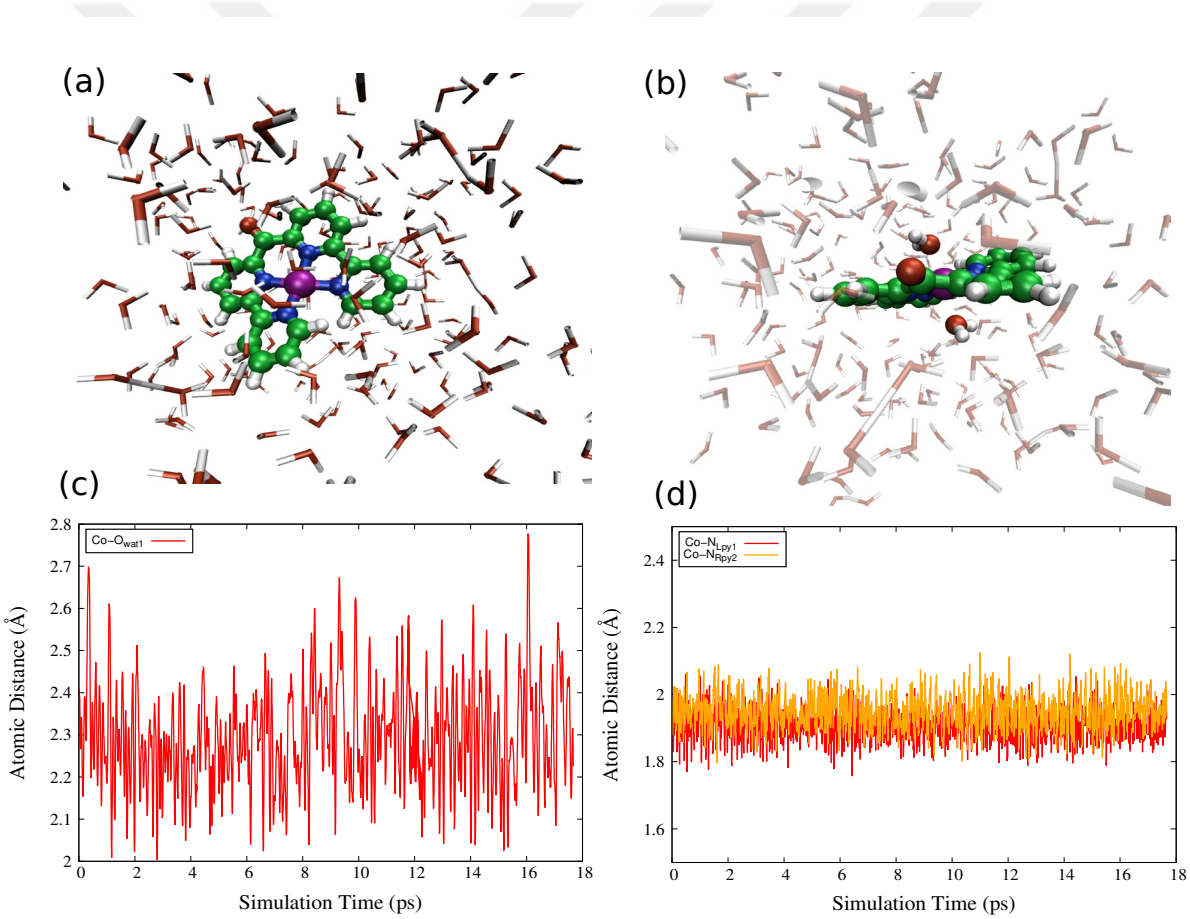

Figure 11: AIMD-NVT simulations for the initial state of the $^{2}(Co(bPy)_2CO)^{+2}$ catalyst. Two views of the catalyst/water from different perspectives (a) and (b) are obtained at 17.67 ps. (c) Interatomic distances between Co and O_{wat1} and (d) atomic distances between Co and surrounding N atoms.

The first intermediate step of the reaction considering the EECC reaction mechanism is the first electron injection to the Co center. As a result of the electron injection the multiplicity of the catalyst/water system can be either singlet or triplet and we carry out AIMD-NVT simulations for both spin states in order to determine the most reasonable spin state for continuing the water reduction reaction. The results for the triplet spin state are depicted in Figure 12-(a). AIMD-NVT simulations have been carried out up to 16 ps and during this time O_{wat1} and O_{wat2} atoms are strongly bonded to the Co center as in the case of the initial state. While the mean Co-O_{wat1} or Co-O_{wat2} distances are fluctuating around 2.25 Å during the simulations of the initial state, these distances increase slightly following the first electron injection, see Figure 12-(b). The protons of the water molecules in the first solvation shell are distant from the Co center, giving Co-H_{wat3} and Co-H_{wat4} distances around 3.4 Å, see Figure 12-(c). The closest water molecules do not undergo any conformational change during the simulations of the triplet spin state.

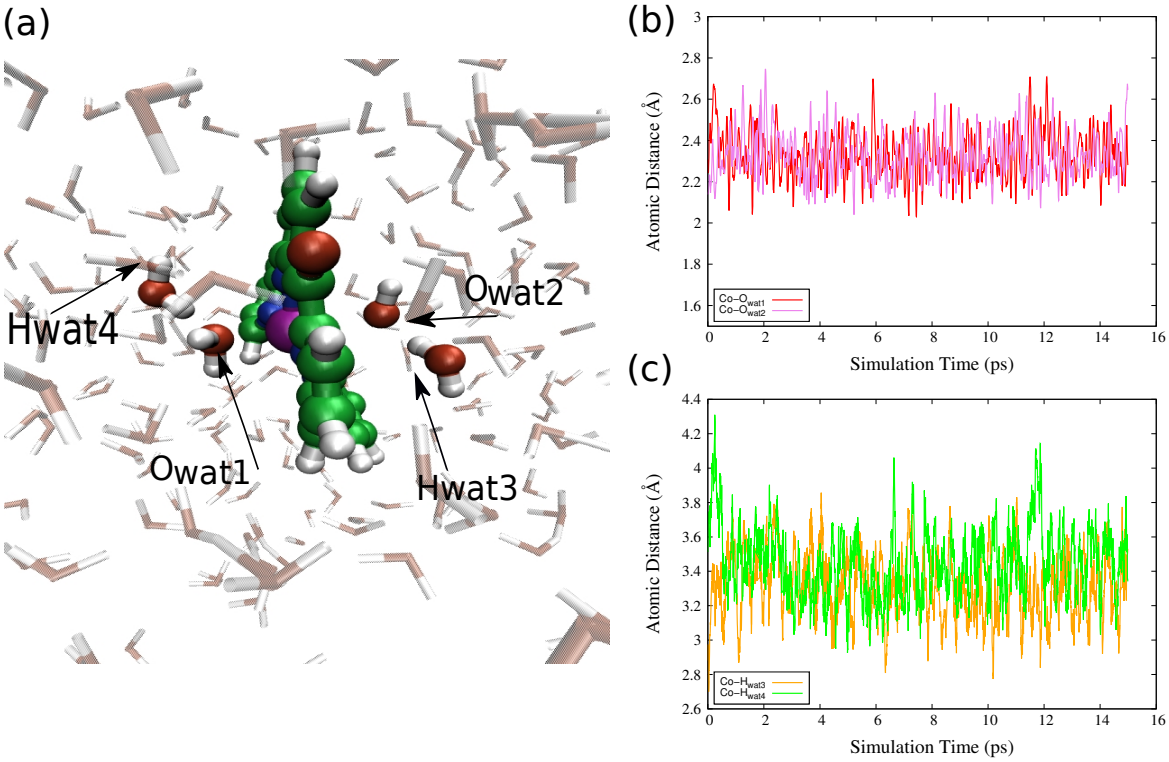

Figure 12: AIMD-NVT simulations for the triplet spin state $^{3}(Co(bPy)_2CO)^{+1}$. (a) A snapshot from the simulation obtained at 15 ps. (b) The distances between Co-O_{wat1} (red) and Co-O_{wat2} (pink) along the AIMD-NVT for the triplet spin state (c) The distances between Co-H_{wat3} (yellow) and Co-H_{wat4} (green) along the AIMD for triplet spin state.

The other possible spin state of the first electron injection is the singlet spin state. Figure 13 shows the results of the simulations carried out using singlet spin multiplicity. AIMD-NVT simulations have been carried out up to 18 ps. During the simulation, water molecules in the first solvation shell keep their coordinates and interact directly with the Co center, similar to the triplet spin multiplicity. Figure 13-(b) shows that the measured distances between the Co and O_{wat1} or O_{wat2} are remarkably similar to those measured in the triplet spin state case (b). Protons that coordinate from the top side to the Co atom are about 3.5 Å distant away from the Co center, as depicted in Figure 13-(c).

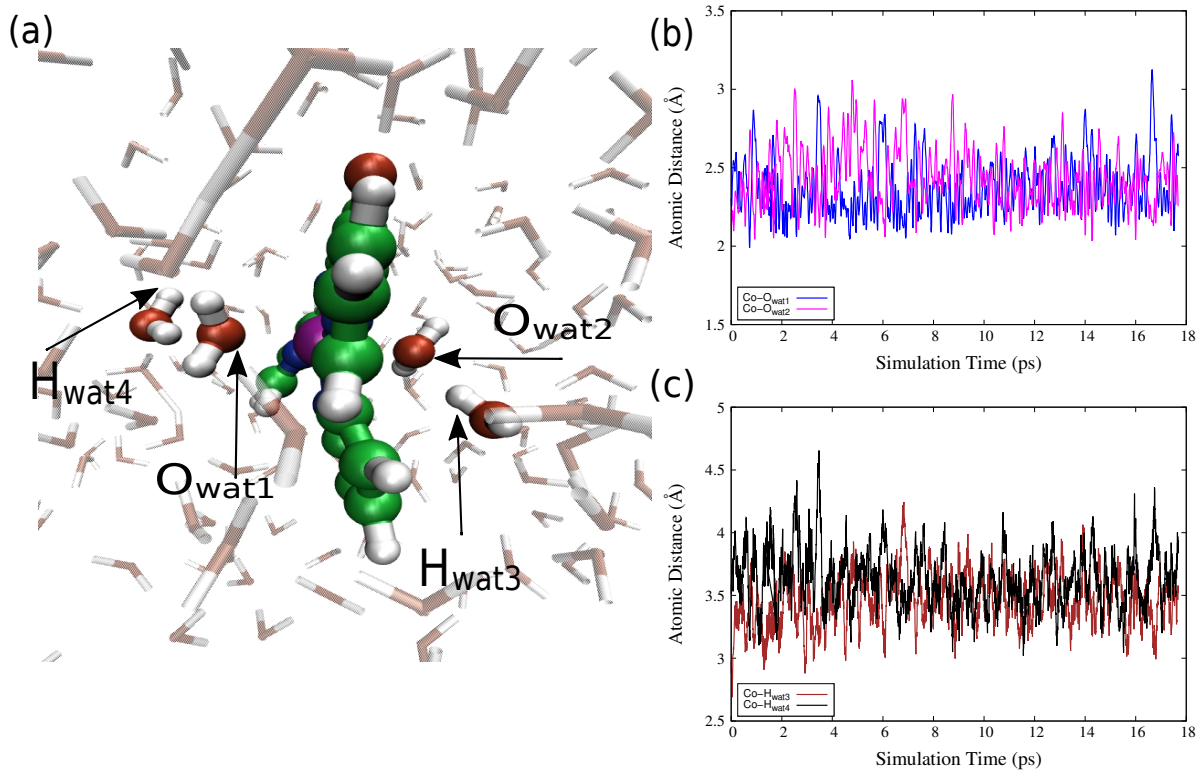

Figure 13: AIMD-NVT simulations of the singlet state $^{1}(Co(bPy)_2CO)^{+1}$. (a) A snapshot from the simulation obtained at 15 ps. (b) The distances between Co-O_{wat1} (blue) and Co-O_{wat2} (pink) along the AIMD for the singlet spin state. (c) The distances between Co-H_{wat3} (red) and Co-H_{wat4} (black) along the AIMD simulation.

The reduction reaction, which is the first step of the H_2 generation reaction for $Co(bPy)_2CO$, is modeled with both triplet and singlet spin multiplicities of approximately 18 ps. After the first electron injection, for both triplet and singlet spin states no change was observed in the bonding geometries of the water molecules, which provide close coordination with the Co center. These results show that there is an energy barrier for water molecules to change their conformation with respect to the Co center which might not be overcome by AIMD simulations. We couldn't observe direct coordination of water proton with Co for both triplet and singlet spin states, thus it can be a rare event that couldn't be sampled by AIMD due to the large energy barrier.

As a result, for the $Co(bPy)_2CO$, it could not be determined using AIMD simulations with which spin state the reaction should continue to the next step. Hence, we use Metadynamics

(MTD) simulations in order to increase sampling in Co-H^+ direct coordinations for both triplet and singlet spin states of the first electron injection intermediate step for $Co(bPy)_2CO$.

In molecular simulations, rare events can be studied in a relatively short time using Metadynamic (MTD) simulations. Metadynamics is an atomistic simulation technique that expands the scope of molecular dynamics simulations, making it possible to accelerate conformational transitions between metastable states and predicting the free energy of complex molecular systems (Bussi & Laio, 2020). MTD relies on iteratively filling the system's potential energy with a Gaussian sum centered along the trajectory followed by an appropriately chosen set of collective variables (CVs), thereby forcing the system to move from one energy minimum to the next. Appropriate collective variables for rare events to be observed in the system can be determined by trial and error.

For the $Co(bPy)_2CO$/water system, according to our phase space sampled by AIMD modeling, only the local minimum energy where Co-O direct coordination is provided during the simulation period up to 20 ps. An energy barrier has to be overcome in order for the water molecule to change its conformation and to exemplify the system in which the Co-H^+ bond is established. By determining the appropriate collective variables with MTD simulations, the overcoming the energy barrier can be accelerated, both states can be exemplified. Besides, the free energy changes of both states having local energy minimums can be calculated.

As a summary, the MTD method allows us to capture the rare events by encouraging the trajectories to visit previously unexplored regions of phase space. Our aim is to carry out simulations for rare events by introducing various collective variables (CV) into the simulation, so that direct coordination of Co and water protons in planar catalyst can be captured and sampled.

In the simulations, the coordination number between Co and the nearest two H is given as a collective variable. When the Hs are close to Co, the coordination number is 2, and when they are farther away, the coordination number is 0. In the MTD simulations, the collective variables are given to increase the coordination number between Co and specified H, thus encourage the sampling of Co-proton direct coordination.

MTD simulations run for the singlet spin state are depicted in Figure 14-(a) and (b). At the starting of the MTD, oxygens have direct coordination with Co. As MTD simulations

prolong, we see that water molecules changes their coordinations and protons are coordinating with the Co center. However, H_{wat1} and H_{wat2} periodically approach and move away from the Co center. At 0.3 ps, Co-H_{wat1} and Co-H_{wat2} decrease to 1.5 Å, while at 0.6 ps corresponding distances increase to 3.5 Å. The hydrogens spend more time away from the Co atom and they change their conformation again as soon as their distance with Co decreases to 1.5 Å.

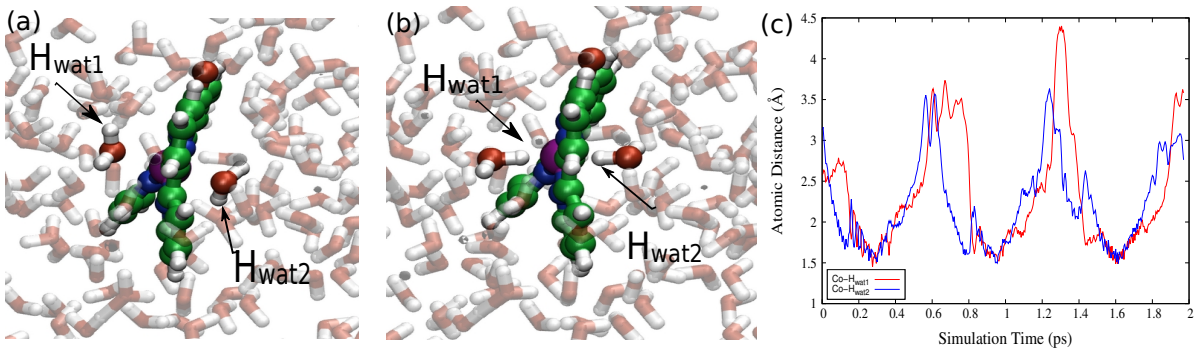

Figure 14: A snapshot from the MTD trajectory for the $^{1}(Co(bPy)_2CO)^{+1}$ system (a) obtained at the 0.1 ps simulation time and (b) 0.27 ps simulation time. (c) Interatomic distances between Co-H_{wat1}(red) and Co-H_{wat2}(blue).

The results of the MTD simulations for the triplet spin state is provided in Figure 15. As in the case of singlet spin state, the distances between Co-H_{wat3} and Co-H_{wat4} oscillates between 1.5 Å and around 3 Å, as depicted in Figure 15- (c). Throughout the simulation, H_{wat3} and H_{wat4} simultaneously approach and move away from the Co center periodically and show the same fluctuating behavior as in the singlet spin state case. At around 0.3 ps, the Co-H_{wat3} and Co-H_{wat4} distances decrease to 1.5 Å, while at 0.6 ps the distances again increase to 3 Å. Similarly, it is seen that the distances decrease to 1.5 Å at 0.9 ps. The reason for the increase in the Co-H_{wat3} and Co-H_{wat4} distances is the establishment of direct coordination between the O_{wat3} (O_{wat4}) and the Co center. The other protons in the solvent do not reach to the Co.

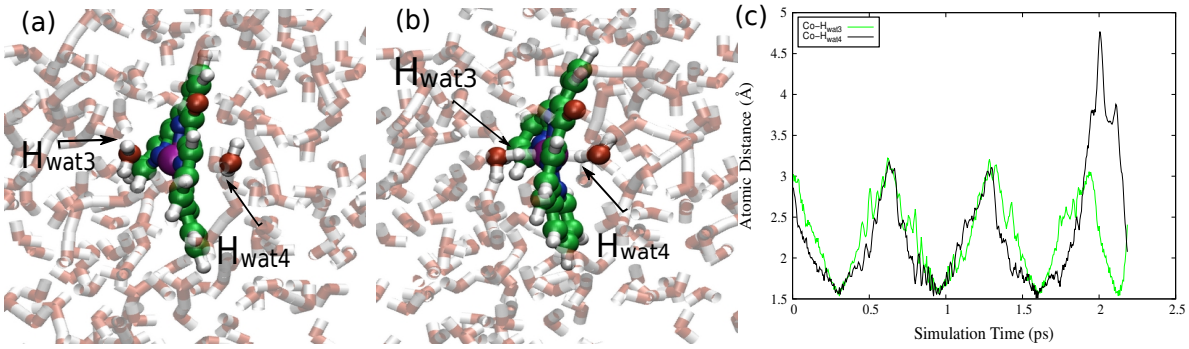

Figure 15: A snapshot from the MTD trajectory for the $^{3}(Co(bPy)_2CO)^{+1}$ system (a) obtained at the 0.1 ps simulation time and (b) 0.3 ps simulation time. (c) Interatomic distances between Co-H_{wat3}(green) and Co-H_{wat4}(black).

As a result of the MTD simulations applied to the singlet and triplet spin states, the hydrogens spent more time away from Co in both spin states and changed their conformation again as soon as their distance from Co decreased to 1.5 Å. In fact, 5 ps is not sufficient for the interpretation of the MTD simulations, however, the results show that the coordination of oxygens in water molecules with Co is more stable in planar Co catalysts. It can be concluded that there is an energy barrier that cannot be overcome during the 17 ps time with AIMD simulations to ensure the Co-H coordination after a conformational change.

In MTD simulations, on the other hand, it was determined that the state where the coordination number between Co-H is 2 (distances of 1.5 Å) is less likely than the Co-O direct coordination state. There is a continuous fluctuation in the distances and the systems spend very little time when the Co-H distance is 1.5 Å and the distances increase immediately after a few MTD steps. In this case, it can be concluded that the probability of states with high Co-H coordination is small, thus states with high Co-H coordination have higher free energy than states with direct Co-O coordination.

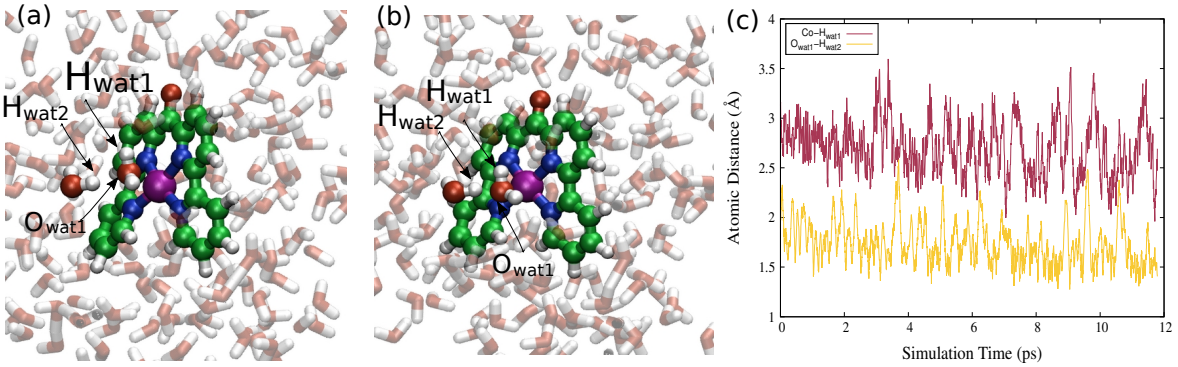

Figure 16: A snapshot from the MTD trajectory with different 2 collective variables for the $^{1}(Co(bPy)_2CO)^{+1}$ system (a) obtained at the 0.1 ps simulation time and (b) 12 ps simulation time. (c) Interatomic distances between Co-H_{wat1}(brown) and O_{wat1}-H_{wat2}(yellow).

MTD simulations for singlet spin state are again performed by changing the collective variable (CV) from Co-H^+ coordination to Co-H_{wat1} and O_{wat2}-H_{wat1} coordination numbers. Snapshots and measured distances are given in Figure 16. In this new MTD simulations, thus two CV have been determined where Co-H_{wat1} coordination is defined as CV1, and O_{wat2}-H_{wat1} coordination is defined as CV2. The simulation run for approximately 12 ps. In the snapshot given at the beginning of the simulation (see Figure 16-(a)), the distance between Co-H_{wat1} is measured as 3.13 Å. There is no interaction between Co and H_{wat1}. According to the Figure 16-(c), the fluctuations continue between 2.5 Å and 3 Å during the simulation time. While the Co-H_{wat1} distance was measured as a maximum of 3.5 Å at approximately 4 ps, the distance decrease to 2 Å at 7 ps. At the end of the simulation (see Figure 16-(b)) close Co-H_{wat1} coordination could not be achieved after 12 ps. The distance between Co-O_{wat1} is measured as 1.89 Å when the simulation beginning. The Co and water molecule are already in direct interaction, and we observe small fluctuations in the measured O_{wat1}-H_{wat2} distance. According to Figure 16-(c), the fluctuations range between 1.5 Å and 2 Å. The direct coordination of H_{wat2}-O_{wat1} prevents its interaction with other water molecules in the simulation box. This should, in fact, be an advantage for establishing direct Co-H_{wat1} coordination which is the main aim for selecting these CVs. We will continue our MTD simulations using these CVs, since direct Co-H^+ can be established if the MTD simulations prolong sufficiently long. Our aim is to calculate free energy difference between Co-O direct coordination and the Co-proton

direct coordination states, so that we can determine rate limiting step of the water reduction reactions catalyzed by planar Co-based bi-pyridyl catalysts.

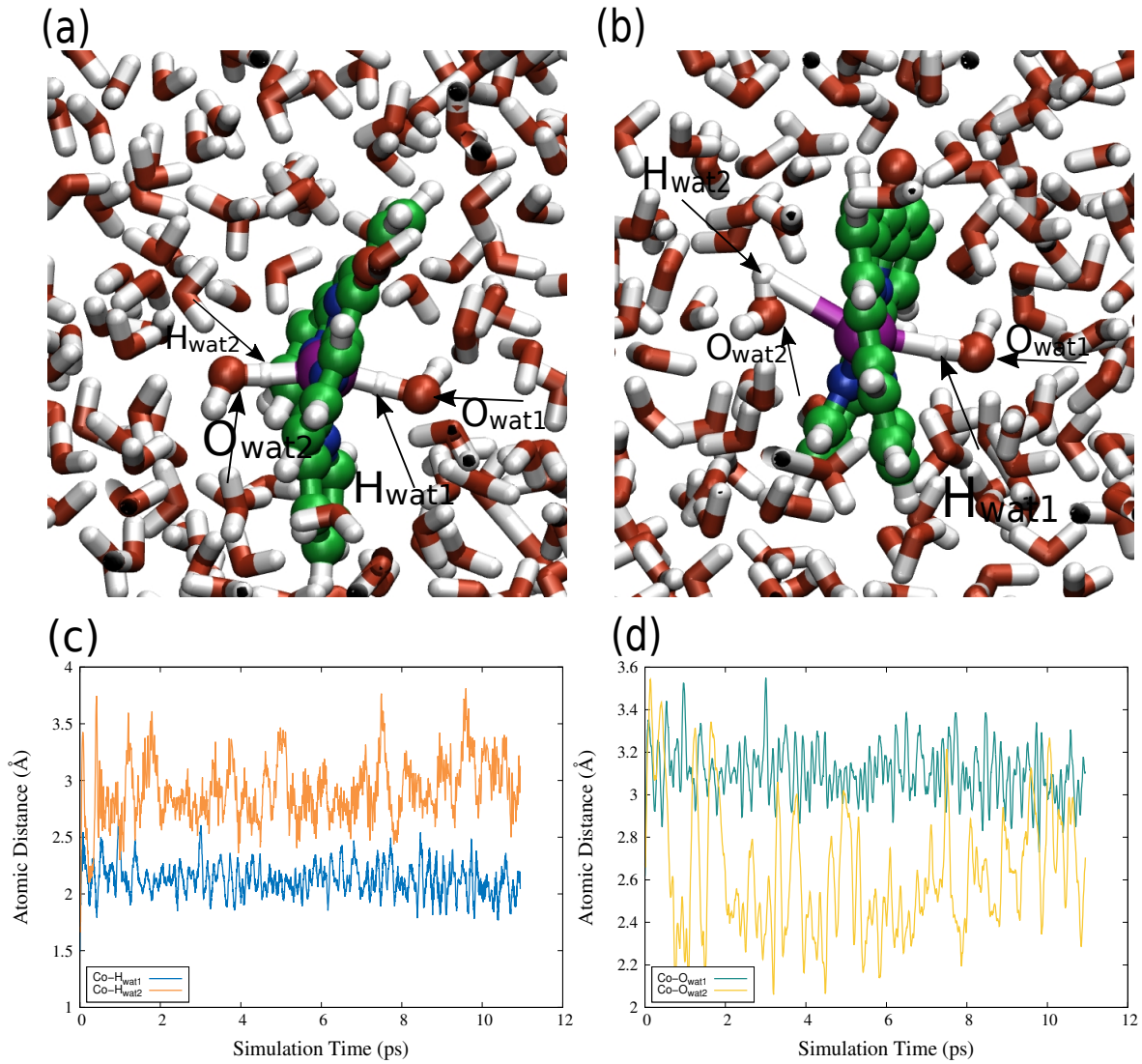

Figure 17: AIMD-NVT simulations for the second electron injection state of the $^{2}(Co(bPy)_2CO)^0$ (a) initial configuration and (b) a snapshot obtained at 10 ps. (c) Interatomic distances between Co and selected H atoms and (d) interatomic distances between Co and selected O atoms of the solvent.

The second intermediate step of the reaction is the second electron injection to the Co center and simulations are carried out for doublet spin state of the system. The snapshots for the doublet spin state which are taken at the initial state of the system and after 10 ps of simulation time are depicted in Figure 17-(a) and Figure 17-(b), respectively. AIMD-NVT simulations have been carried out up to 10 ps so far. The initial configuration of the system has been taken from the MTD simulations where direct Co-proton coordinations have been established. At the beginning of the simulation, H_{wat1} and H_{wat2} keep their coordinates and interact directly with the Co center. However, as AIMD-NVT simulations evolve we observe large fluctuations in the Co-H_{wat2}, see Figure 17-(c), and its distance reaches to 3 Å implying one of the Co-proton coordination is broken. Considering Co-H_{wat1} coordination, on the other hand, its distance is measured around 2 Å. This means, while Co-H_{wat1} coordination is broken, systems preserves Co-H_{wat2} coordination which is reason of more negative Co center compared to the first electron injection step. Preserving Co-H_{wat2} coordination is a promising result, since Co can take this proton for the first protonation intermediate step of the reaction. Figure 17-(d) shows the measured distances between the Co and O_{wat1} and O_{wat2}. The Co-O_{wat2} distance fluctuates largely between 2 Å and 4 Å throughout the simulation. The distance, which is about 3 Å at the beginning of the simulation, decreases to 2 Å in 2 ps and the Co-O_{wat2} direct coordination is observed. The Co-O_{wat1} interaction, on the other hand, is stable at around 3 Å distance. The cobalt atom provides direct coordination with the H_{wat1} proton, and its interaction with the H_{wat2} proton is considerably reduced. During the simulation, the cobalt atom attracts one of the surrounding hydrogens and repels the other. Co and proton (H_{wat1}) are directly coordinated and the coordination state did not change until end of the simulation.

4.1.1 Electronic Structure Analysis

Electronic structure calculations are carried out using the PBE0-rVV10 hybrid density functional using snapshots obtained from AIMD-NVT simulations for the first and second electron injection intermediate steps of the EECC mechanism. The relative position and distribution of the boundary orbitals, namely the highest occupied (HOMO) and the lowest unoccupied (LUMO) molecular orbitals are investigated at different time periods during the simulations.

Figure 18-(a) shows the fluctuations of band gaps of the $Co(bPy)_2CO$ which is defined as the difference between HOMO and LUMO energies calculated for the first electron injection and

the second electron injection steps along the AIMD trajectory. Oscillations in band gaps are calculated for the initial state $^{2}(Catalyst)^{+2}$ (blue), the first electron injection state having triplet spin state $^{3}(Catalyst)^{+1}$ (green) and singlet spin state $^{1}(Catalyst)^{+1}$ (red), and for the second electron injection state $^{2}(Catalyst)^{0}$ (purple). Note that x axis in the Figure 18-(a) shows the production time (data collection time) instead of total simulation timings.

According Figure 18-(a), band gap of the initial state fluctuates around 2.5 eV and 3 eV. Band gap decreases less than to 2 eV in the range of 8-9 ps. After the first electron injection, the two reduced states present similar behavior and show small fluctuations throughout the production time. While triplet state has band gap around 2.2 eV, singlet state has a band gap around 2 eV. After the second electron injection, the band gap decreases by more than 1 eV with respect to the first reduction step, and fluctuates at around 1 eV. It should be keep in mind that these calculations have been performed using hybrid density functional PBE0 plus non-local dispersion functional, rVV10, thus these estimates should be, in principle, more accurate than the estimates obtained by the GGA functionals.

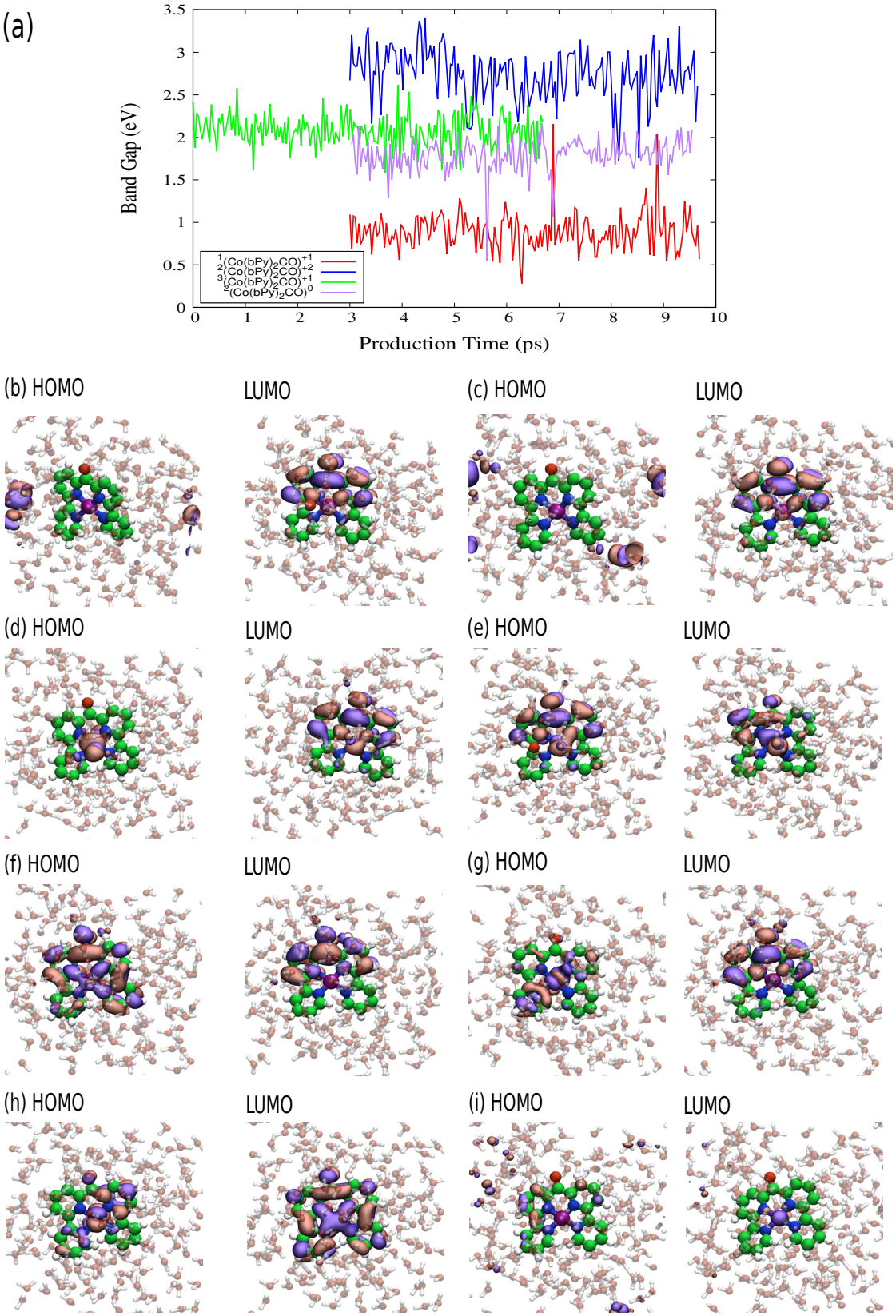

Figure 18: (a) Comparison of band gap energy for all spin state of the catalyst for the first reduction and the second reduction steps. Color code: blue initial state ^{2}(Catalyst)$^{+2}$; green reduced state ^{3}(Catalyst)$^{+1}$; red reduced state ^{1}(Catalyst)$^{+1}$; Purple the second electron injection ^{2}(Catalyst)^{0}.

The HOMO and LUMO distributions obtained for one extracted snapshot for each state: (b) $^{2}(Co(bPy)_2CO)^{+2}$ at 3.26 ps, (c) $^{2}(Co(bPy)_2CO)^{+2}$ at 9.59 ps, (d) $^{1}(Co(bPy)_2CO)^{+1}$ at 0.27 ps, (e) $^{1}(Co(bPy)_2CO)^{+1}$ at 1.29 ps, (f) $^{3}(Co(bPy)_2CO)^{+1}$ at 0.95 ps, (g) $^{3}(Co(bPy)_2CO)^{+1}$ at 1.99 ps, (h) $^{2}(Co(bPy)_2CO)^{0}$ at 0.24 ps, and (i) $^{2}(Co(bPy)_2CO)^{0}$ 5 ps of production time. The isosurfaces corresponds to 0.018 e/Å^3 depicted in pink and -0.018 e/Å^3 in purple.

We carry out molecular orbital distribution analysis for all spin states of the first and the second electron injection steps by selecting snapshots from the AIMD-NVT trajectories. The Figure 18-(b) and (c) show the HOMO and LUMO distributions of initial state of the $(CobPy)_2CO$. For the selected snapshots at 3.26 ps and 9.59 ps production time, HOMO is located on the water molecules rather than the catalyst. LUMO states, on the other hand, are localized on the pyridyl rings. Configurations of singlet and triplet spin states are taken from the MTD trajectories where direct coordination between Co and protons are established. HOMO and LUMO of the singlet spin state are depicted in Figure 18-(d) and (e). For the singlet spin state, it is observed that the HOMO is on the Co and the water molecules in the first solvation shell. The dz^2 orbital of the Co forms HOMO. LUMO is distributed over the pyridine rings of the bipyridine ligands. The molecular orbital distributions of the triplet state are depicted in Figure 18-(f) and (g). For the triplet spin state, it is observed that HOMO is distributed to the pyridine rings of the bipyridine ligands. LUMO, on the other, is located on the bipyridine ligand. From the molecular orbital analysis it is clear that the first protonation step should continue with the singlet spin state where there are states formed by Co and the water molecules.

After the second electron injection, the HOMO is often dispersed over the pyridine rings. LUMO is located on the all atoms of catalyst at the beginning of the simulation, see Figure 18-(h). Then it is distributed over the cobalt and N atoms at 5 ps of the production time, see Figure 18-(i).

4.1.2 Reduction Free Energies

In this section, we compute the reduction free energies for both the first and the second electron injection steps. The reduction free energy of the $Co(bPy)_2CO$ catalyst after the first electron transfer is calculated by the accumulative time averages of the vertical energy gaps, ΔE, of the reduced, $^1(Co(bPy)_2CO)^{+1}$ and the oxidized, $^2(Co(bPy)_2CO)^{+2}$ spin states. The averages of ΔE plotted in Figure 19-(a) are calculated as -3.27 eV and 1.86 eV for the reduced limit ($<\Delta E>_R$) and oxidized limit ($<\Delta E>_O$), respectively. Using Equation 3.4, the reduction free energy of the $Co(bPy)_2CO$ for the first electron injection, $\Delta A_{R\text{-}O}$, is calculated to be -0.71 eV. Also, the reorganization free energy of the first electron injection step is calculated as -2.56 eV, see Table 2. While calculating reduction free energies we use Marcus' theory of electron transfer (Marcus,1956) which assumes that while electron transfer occurs in homogeneous systems, solvent shows linear behavior. While nucleus movement is very slow, electrons are injected very fast, thus linear solvent response should hold. Table 2 shows the calculated values of widths to the Gaussian fits to the averages of vertical energy gaps. If the Gaussian widths are similar to the each other for the reduced (σR) and oxidized limits (σO), the linear solvent response assumption holds and we can use free energy perturbation theory within the Marcus theory of electron transfer. As it can bee seen in the table, Gaussian widths of oxidized and reduced limits are calculated as 0.25 eV and 0.26 eV, respectively, which are similar to each other. Thus, linear solvent assumption holds and the calculated reduction free energy of the first reduction energy is reliable.

Table 2 : For the the first and the second electron injection steps calculated reduction free energies (ΔA_{R-O}), standard deviations for the reduced (σ_R) and oxidized states (σ_O), and reorganization free energies (λ) are summarized. All properties are in eV. For the first electron injection reaction, calculations are carried out only for the singlet spin state.

		$\Delta A_{R\text{-}O}$	σ_R	σ_O	λ
1st reduction free energy	**Singlet Spin State**	-0.71	-3.27	1.86	-2.56
	Triplet Spin State	-0.73	-1.52	0.24	-0.99
2nd reduction free energy		-0.52	-0.72	-0.32	-0.21

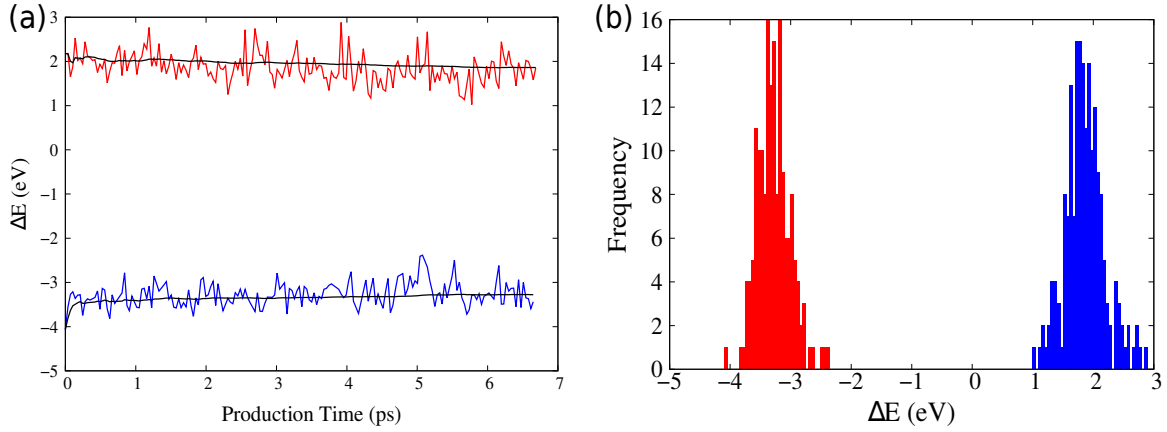

Figure 19: Following the first electron injection, $^{2}(Co(bPy)_2CO)^{+2}$ +e- → $^{1}(Co(bPy)_2CO)^{+1}$ (a) instantaneous and average energy with respect to the production time for singlet spin state. Reduced limit is depicted with blue, the oxidized limit is shown with red solid line and black line refers to ensemble average. (b) Distributions of the vertical energy gaps of the first reduction reaction.

The reduction free energy of the $Co(bPy)_2CO$ catalyst after the first electron injection is calculated by the accumulative time averages of the vertical energy gaps, ΔE, of the reduced, $^{3}(Co(bPy)_2CO)^{+1}$ and the oxidized, $^{2}(Co(bPy)_2CO)^{+2}$ spin states. The averages of ΔE plotted in Figure 20-(a) are calculated as -1.52 eV and 0.24 eV for the reduced limit ($<\Delta E>_R$) and oxidized limit ($<\Delta E>_O$), respectively. Using Equation 3.4, the reduction free energy of the $Co(bPy)_2CO$ for the first electron injection, $\Delta A_{R\text{-}O}$, is calculated to be -0.73 eV. Also, the reorganization free energy of the first electron injection triplet spin step is calculated as -0.99 eV, see Table 2. Moreover, as it can bee seen in the table, Gaussian widths of oxidized and reduced limits are calculated as 0.15 eV and 0.15 eV, respectively, which are similar to each other. Thus, linear solvent assumption holds and the calculated reduction free energy of the first reduction energy is reliable. The reduction free energy for triplet spin state is less negative than the corresponding value calculated for the singlet spin state. For reduction free energy calculations, a more negative reduction free energy value means that the system needs more energy to get electrons. Thus, the energy requirement for getting the triplet spin state is

0.02 eV more than the energy required for getting the singlet spin state. Thus, from reduction free energy calculations, proceeding the reaction with singlet spin state is, in principle, slightly more favorable.

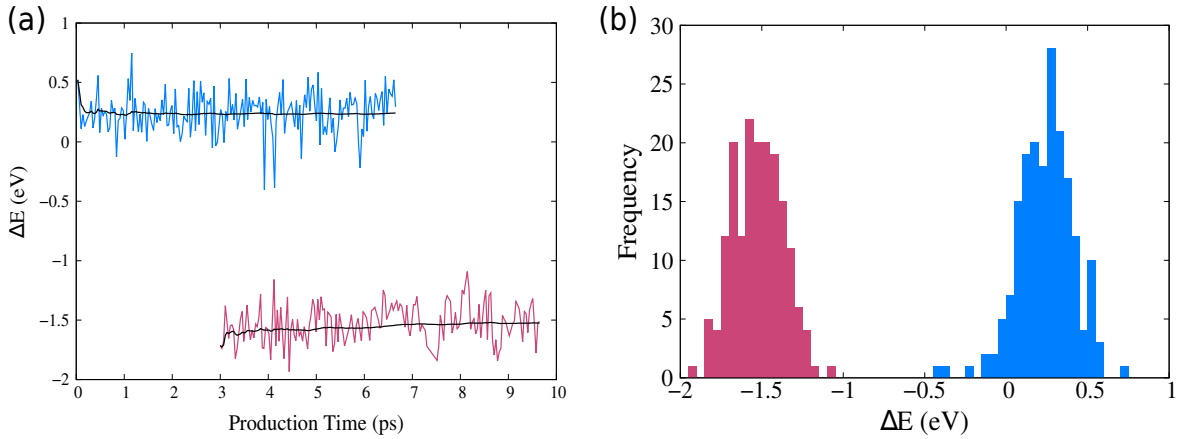

Figure 20: Following the first electron injection, $^{3}(Co(bPy)_2CO)^{+1}$ +e- → $^{2}(Co(bPy)_2CO)^{+2}$ (a) instantaneous and average energy with respect to the production time graph for triplet spin state. Reduced limit is depicted with blue, oxidized limit is shown with pink solid line and black line refers to ensemble average. (b) Distributions of the vertical energy gaps of the first reduction reaction.

Following the second electron injection, reduction free energy of the $Co(bPy)_2CO$ catalyst is calculated by the accumulative time averages of the vertical energy gaps, ΔE of the oxidized $^{1}(Co(bPy)_2CO)^{+1}$ and reduced $^{2}(Co(bPy)_2CO)^{0}$ states. While the reduced, $\langle\Delta E\rangle_R$ limit is calculated as -0.72 eV, oxidized, $\langle\Delta E\rangle_O$ limit is calculated as -0.32 eV, (see Figure 21). As a result, the second reduction free energy of the $Co(bPy)_2CO$, $\Delta A_{R\text{-}O}$, is calculated as -0.52 eV. Also, the reorganization free energies are calculated as -0.21 eV. After the second reduction free energy calculations, the $\Delta A_{R\text{-}O}$ value decreases with respect to the reduction free energy of the first electron injection reaction. The second reduction free energy is less negative than the first reduction free-energy. In reduction free energy calculations, a more negative reduction free energy value means that the system needs more energy to get electrons. Thus, the energy requirement for getting the first electron is 0.19 eV more than the energy required for getting the second electron.

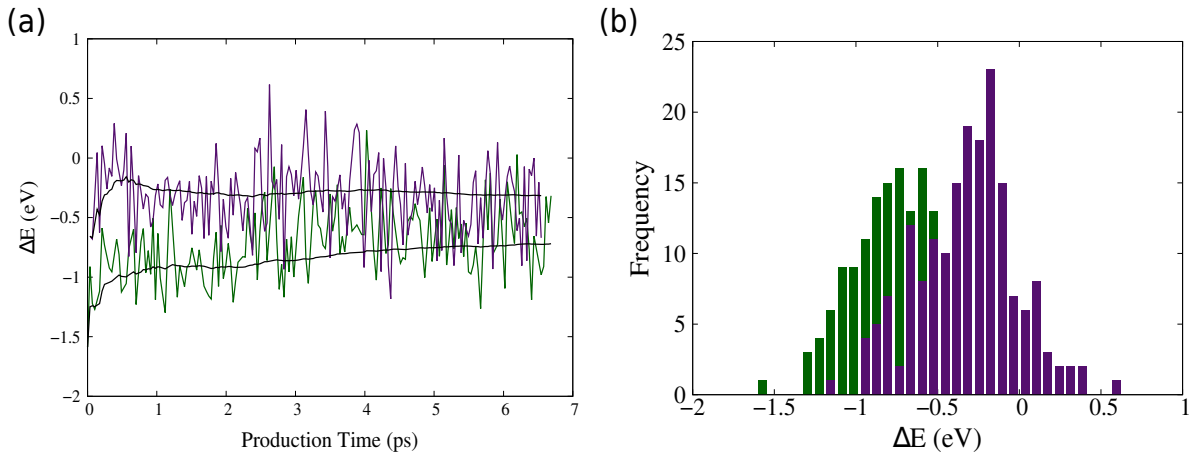

Figure 21: Following the second electron injection, $^{1}(Co(bPy)_2CO)^{+1}$ +e- → $^{2}(Co(bPy)_2CO)^{0}$ (a) instantaneous and average energy with respect to the production time for doublet spin state. While reduced limit is shown with green, oxidized limit is depicted with purple solid line and black line refers to ensemble average. (b) Distributions of the vertical energy gaps of the first reduction reaction.

The spin multiplicity calculation is carried out in order to verify which spin state the system is in. It is calculated by the number of half-filled orbitals of Cobalt. (Eq. 3.7)

$$Spin\,multiplicity = 2x\frac{half-filled\,orbital\,number}{2}+1 \qquad (3.7)$$

According to the Equation 3.7, Cobalt must have no half-filled orbitals for the singlet spin state. In the case of doublet spin, 1 half-filled orbital gives the spin multiplicity 2. In the Ab-initio MD systems, the spin moment of Cobalt demonstrates that the system have been running with the correct spin state, see Figure 22.

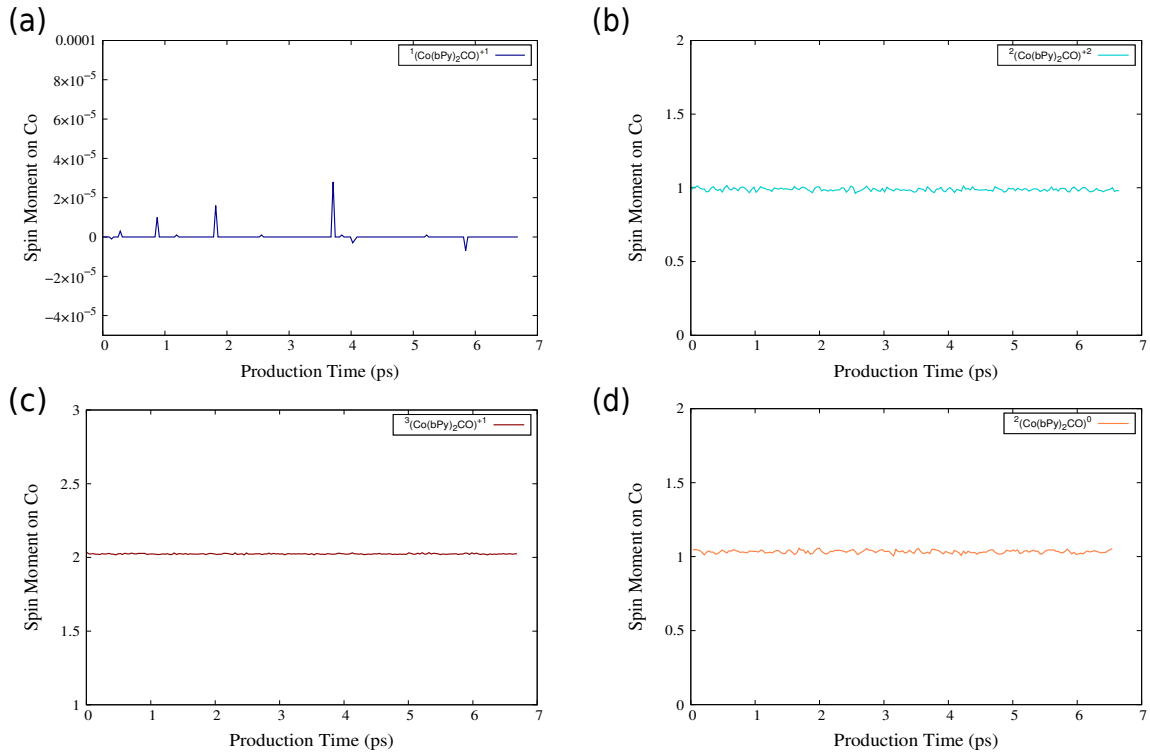

Figure 22: Spin moment of Cobalt with respect to the production time for the first reduction state(singlet spin state) (a), for the initial state of the catalyst (b), for the first reduction state (triplet spin state) (c), and for the second reduction state (d).

4.2 Adsorption of Co-based Water Reduction Catalysts on Rutile(110)

In this section, we investigate the adsorption of cobalt-centered water reduction catalysts on the TiO_2 (110) surface by means DFT. The catalysts investigated in this section have been previously shown as promising candidates for H_2 production through water reduction reaction (WRC). The information of the catalysts under consideration are already given in the Materials and Methods section. (Schnidrig et al., 2017) experimentally investigated the H_2 generation performances of several poly-pyridyl catalysts including $Co(bPy)_2CO$ **(Cat1)**. It has been shown that $Co(bPy)_2CO$ exhibits high stability during the reaction and it has a reaction rate of 20 nmol H_2/s under optimum conditions. (Joliat-Wick et al., 2018) investigated the H_2 generation performances of $Co(bPy)_2(CO)_2$ catalyst having two bi-pyridyl and one di-ketone groups **(Cat2)** in the planar structure. It has been shown that $Co(bPy)_2(CO)_2$ reaches a reaction rate of 60 nmol/s under optimum conditions. (Varma et al., 2013) examined the photo-catalytic H_2 production properties of $[Co(CR)Cl_2]$ + cobalt(III) tetraaza-macrocyclic molecule **(Cat3)** in aqueous solution. Observed in acetonitrile solution, the greater catalytic performance of the PS/Cat3 system have be attributed to the strong stability of the low-valent Co(I) oxidation state in the tetraaza-macrocyclic catalyst. (Queyriaux et al., 2018) investigated the hydrogen production performance of the new cobalt tetrapyridyl complex **(Cat4)** in aqueous solution. The reaction occurs in an environment of pH 4.5. In system that proceeds with the ECEC mechanism and under acidic conditions, the results show that the catalyst under consideration has an active role in hydrogen production, producing 443 TONs – 3 mL of H_2 in aqueous solution.

We first run the geometry optimization of four planar WRC catalysts using the DFT method. TiO_2 is modeled suing 5 layers slab model where top 2 layers are relaxed during the simulations and the bottom 3 layers are kept fixed at bulk positions. Periodic boundary conditions are applied in all three directions. After adsorption of the catalysts on the TiO_2 surface, 20 Å vacuum distance is applied along the surface normal in order to prevent interactions of the molecule and the bottom layer of the material. The catalysts are attached to the rutile surface at a distance of 5 Å before running the geometry optimization. The central Co atom of the catalysts are located in coordination with the surface Ti or O atoms. Figure 23 shows the optimized geometries of the catalysts/TiO_2 systems. Calculated adsorption and dispersion energies are reported in Table 3.

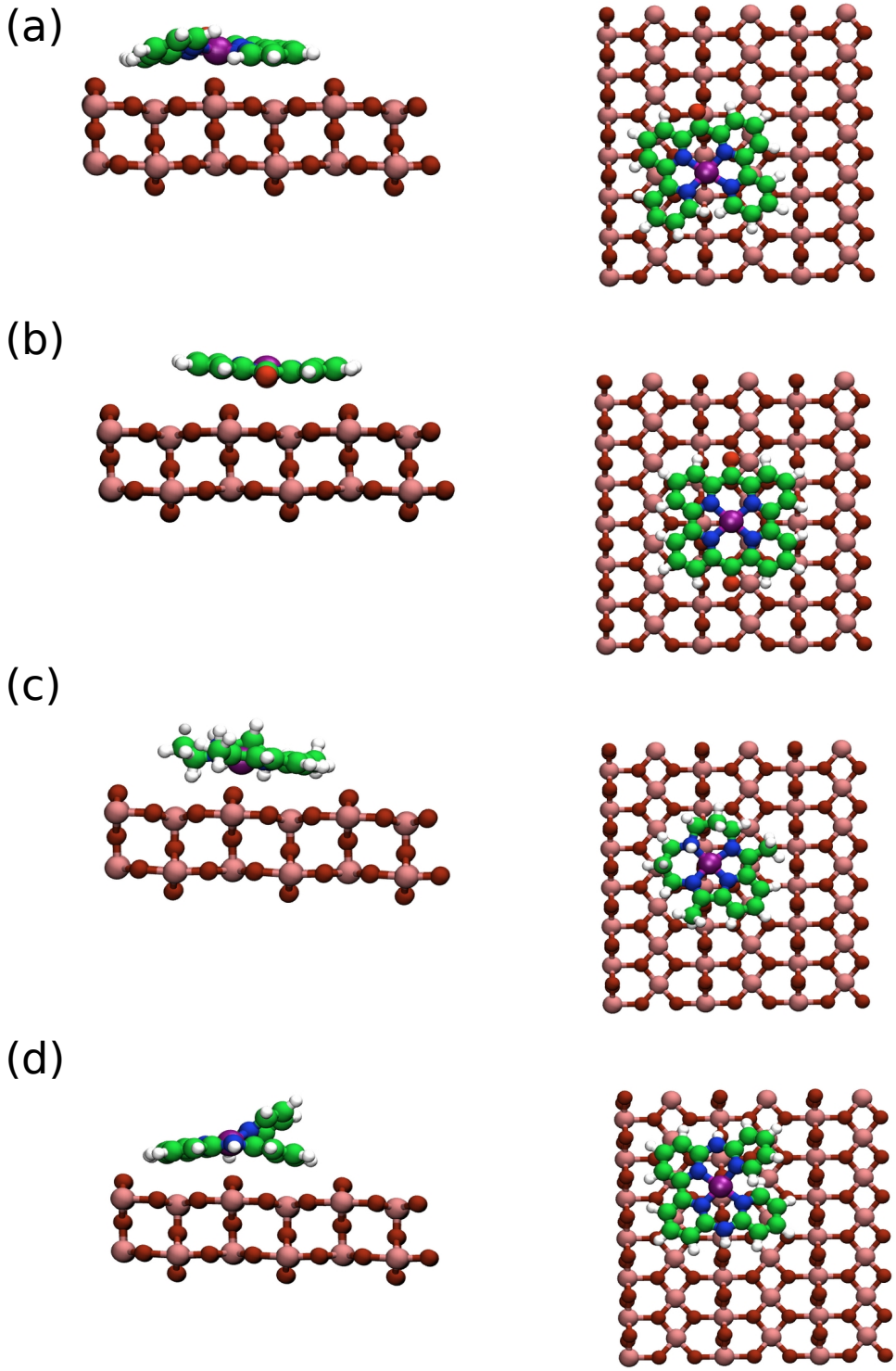

Figure 23: TiO_2 complexes with four different optimized catalyst configurations. Each of the four models is shown from the top (left) and one side (right). Color code: pink: Ti, red: O, blue: N, green: C, white: H, purple: Co

Figure 23-(a) shows the top and side view of the planar $Co(bPy)_2CO$ **Cat1** catalyst attached to the rutile 110 surface at a distance of 6 Å. The pyridine rings coordinate with the 5 coordinated surface Ti_{5c} and 3-coordinated surface O_{3c} atoms. While the oxygen in the backbone of the catalyst coordinates with 6-coordinated surface Ti_{6c} atom, the distance between them decreases to 4 Å at the end of the simulation. The pyridine rings are distorted during the simulation and planar structure of the catalyst is deformed which facilitates interaction between the surface and the molecule. The strong interaction between Co and O_{3c} results in having reduced bond length as 2 Å. As a result of the optimization, the adsorption energy is calculated as -16.45 eV of which -2.73 eV is attributed to dispersion energy.

The adsorption of Co diketo-Pyrphyrin **Cat2** catalyst on the surface, in which pyridine rings are bonded with two oxygen atoms is shown in Figure 23-(b). Co-O_{3c} distance is measured as 4.97 Å at the beginning of the simulation. Pyridine rings are interacting with surface oxygens. O-H and C-O coordination are frequently seen. Diketo groups are attached to the surface in such a way that they do not have close interaction with any atom on the surface at the beginning of the simulation. When the geometry optimization is completed, the diketo oxygens' are bent towards the Ti_{5c} atoms, however the catalyst preserves the planar geometry. Average atomic distances decrease to about 4 Å as in the Co-O_{3c} coordination. The adsorption energy of the system is calculated as -18.88 eV. Although, adsorption energy is higher than model a, dispersion energy is smaller which is calculated as -2.21 eV.

Figure 23-(c) shows Co-O_{2c} interaction in Cobalt tetraaza-macrocyclic **Cat3** adsorption. The catalyst rotates during the geometry optimization. In the catalyst with a single pyridine ring and many hydrogen atoms, the hydrogen atoms are directed towards the surface oxygens. Adsorption is completed with an atomic distance of 2.12 Å between Co-O_{2c}. Adsorption energy is calculated as -9.47 eV. Compared with the other catalysts, the lowest adsorption energy is calculated for the model show in (c) $[Co^{III}(CR)Cl_2]^+$. Both adsorption and dispersion energies are smaller for model (c) which respect to the other models.

For the Cobalt tetrapyridyl complex **Cat4**, Co-Ti_{6c} direct coordination is seen in Figure 23-(d). In the catalyst with a four pyridine ring, Cobalt atom is placed on top of the O_{3c} atom on the surface. The interaction of the atoms repulse the cobalt central on top of the Ti_{6c} surface atom. The hydrogen atoms coordinate with the O_{3c} atoms. While the three pyridine rings preserve

their planar structure on the surface, the single pyridine ring is sticking out from the surface due to the repulsion forces. When Co-Ti_{6c} coordination is achieved with a distance of 3.78 Å, the adsorption energy of the system is calculated as -16.91 eV. Besides, dispersion energy is calculated as -2.5 eV.

Table 3 : Adsorption and dispersion energies of the planar Co based catalysts and their atomic coordination

Model	**Catalyst**	**E_{ads} (eV)**	**E_{disp} (eV)**	**Pair**
a	$Co(bPy)_2CO$ (**Cat1)**	-16.45	-2.73	Co-O_{2c}
b	Co diketo-Pyrphyrin**(Cat2)**	-18.88	-2.21	Co-O_{3c}
c	$[Co^{III}(CR)Cl_2]^+$**(Cat3)**	-9.47	-2.15	Co-O_{2c}
d	Cobalt tetrapyridyl complex **(Cat4)**	-16.91	-2.5	Co-Ti_{6c}

The atomic coordinate pairs and adsorption energies of the catalysts are summarized in Table 3. The calculated adsorption energies are rather high and the reason is attributed to the dominated chemical interactions between catalysts and the surface. Besides, the structures of the catalysts on the surface significantly divert from their geometries in the homogeneous environment. The lowest adsorption energy is obtained in model-(c). We continue electronic structure analysis which is carried out only for the model-(c). The reason is that these catalysts show WRC activity in homogeneous environments and their strong adsorption on the material surfaces which affect their geometries might also affect their WRC performances. Thus, model-(c), $[Co^{III}(CR)Cl_2]^+$ catalyst, which gives the least adsorption energy is selected for further analysis. In order to increase accuracy, HSE06 hybrid density functional together with Grimme-D3 correction has been performed.

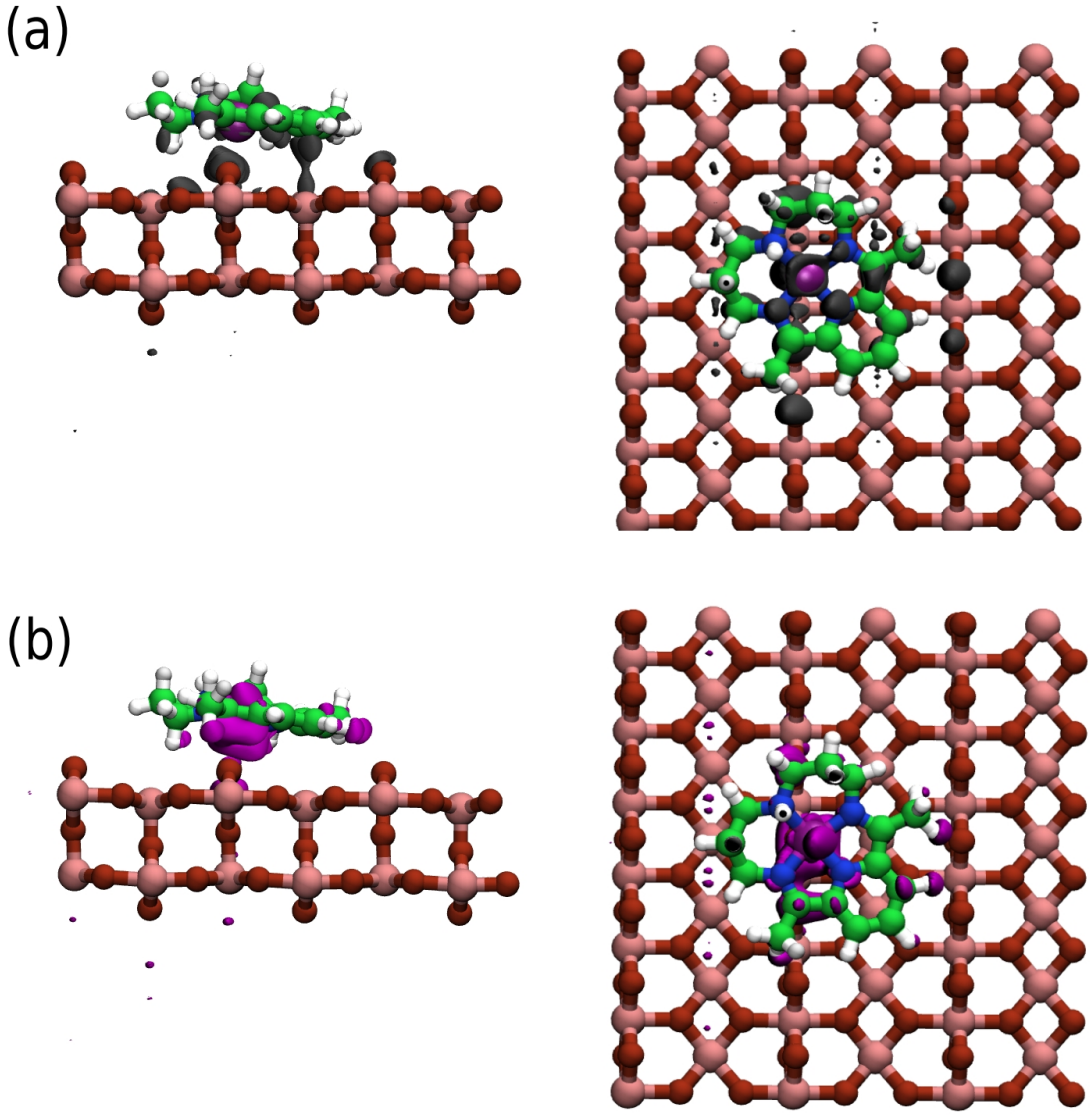

Figure 24: Electronic density analysis of $[Co^{III}(CR)Cl_2]^+$/rutile(110) from front view (left panel) and from top view(right panel) The isosurfaces corresponds to 0.001 e/Å^3 depicted in gray (a) and -0.001 e/Å^3 in purple (b).

Figure 24 shows the two electronic density difference isosurfaces, Δρ(r), corresponding to −0.001 e/Å^3 , i.e., charge depletion (bottom model) and +0.001 e/Å^3 , i.e., charge accumulation (top model), for $[Co^{III}(CR)Cl_2]^+$/rutile(110). The electron density is distributed between the pyridine rings and Ti_{5c} and O_{2c}. Herein, electron accumulation is observed in these regions. This explains the chemical interactions between the pyridine rings and the Ti and O atoms. Figure 24-(b) shows the electron depletion between the O_{2c} atom and central

cobalt atom and N atoms. Rather, there has been a transfer of electrons from the catalyst to the surface atoms. This is mostly observed on Co and surrounding N atoms.

5 CONCLUSIONS

In the first part of this thesis, we investigate the hydrogen production mechanism of a cobalt-based Co(bPy)CO catalyst having a planar structure in explicit water environment. EECC reaction mechanism for water reduction is investigated and AIMD simulations have been carried out for the first and the second electron injection steps. By observing the solvent response and structural changes that take place at the reduction steps of the catalytic cycle, the impacts of planar structure and the coordination environment surrounding the Co center on the reaction mechanism have been studied. To this aim, reduction steps have been modeled using AIMD simulations in the GGA-PBE formalism and trajectories have been obtained approximately 20 picoseconds. We calculate the reduction free energy changes for both reduction reactions using the free energy perturbation theory, Marcus electron transfer theory and linear solvent response assumption. While trajectories are obtained using PBE density functional, reduction free energies are calculated by selecting more than 200 snapshots from the AIMD trajectories and applying PBE0 density functional together with rVV10 dispersion functional.

$Co(bPy)_2CO$ catalyst has doublet spin state at the beginning of the reaction. Following the first electron injection, which is the first intermediate step of the EECC mechanism, singlet or triplet spin states can be formed. We have not observed any conformational change of the water molecules in the first solvation shell during the AIMD simulations of both triplet and singlet states. Results suggest that in contrast to the Co based catalysts having an octahedral arrangement (Bachman and Alberto et al., 2013), establishing direct Co-proton bond in planar catalysts requires an energy barrier which could not be sampled by AIMD simulations. We perform two MTD simulations having different Cvs. In the first MTD the coordination number between Co and the hydrogens are selected as CV. Co-H bonded states have been sampled, however the probability of these states are low, which also suggests that the presence of a large free energy difference between Co-O and Co-H bonded states. We observe continuous breaking and formation of Co-H coordination during the MTD run. As a second MTD simulation, the coordination between Co-H (the closest H bonded to O_{wat1}) and coordination number between the solvent oxygen and the other H bonded to O_{wat1} are selected as CV in order to prevent continuous rotation of the closest water molecule and breaking of Co-H coordination, as in the first MTD. During the second MTD simulations, we observe

decreasing distance between Co and the H_{wat1} which occurs slowly. The simulations have been performed for 12 ps which will continue at least for 20 ps, since in 12 ps we could not observe direct coordination between Co and the H_{wat1}. Calculation of HOMO and LUMO states of the first reduction step suggests that the system is more likely to continue to the second reduction reaction with the singlet spin state.

After the second electron injection, one of the closest proton is bonded with the cobalt and remains stable throughout the simulation. While the other proton has decreased coordination with cobalt and turned towards to the solvent. The trajectory suggests that the required proton for the first protonation step is more likely to be provided by the water molecule having direct Co-H coordination.

Reduction free energy for first reduction reaction is calculated as -0.71 eV. For the second step, reduction free energy is computed as -0.52 eV. Compared to both steps, first free reduction energy is more negative, meaning the first reaction step needs more energy than the second reaction step for electron transfer.

In the second part of this thesis, we study adsorption of different planar Co-based catalysts on TiO_2 rutile(110) surface. The interactions of planar cobalt-based catalysts containing different pyridyl rings with surface atoms have been investigated. The energies and structural changes of the catalysts following the adsorption have been compared. While geometry optimizations are completed applying PBE density functional together with Grimme-D3 correction, further electronic density difference analysis of the selected complex has been performed using HSE06 hybrid density functional in order to increase the accuracy in modeling molecular catalyst and semiconductor complex.

Following the geometry optimization calculations, we observe deformations in the planar structures of the catalysts under consideration which are resulted due to increase chemical and physical interactions between the molecules and the surface. Calculated adsorption energies are rather large, which suggests that chemical interactions between the catalyst and the surface dominate. Electron density difference maps show that there is electron exchange between Co center and the surface oxygens. In addition, interactions are observed between pyridyl nitrogen atoms and surface atoms.

With this thesis, we intend to expand the current knowledge on the hydrogen generation performances of cobalt-based catalysts having planar structure in homogeneous and

heterogeneous environments. We characterize the first and the second reduction intermediate steps of the EECC reaction mechanism held in water solution. Adsorption geometries of the several Co based planar catalysts are stabilized on the TiO_2 surface.

REFERENCES

Alberto, R., Guttentag, M., & Spingler, B. (2013). 3d Element complexes of pentadentate bipyridine-pyridine-based ligand scaffolds: Structures and photocatalytic activities. *Inorganic Chemistry*, *52*(10), 6055–6061.

Ambrosio, F., Miceli, G., & Pasquarello, A. (2015). Redox levels in aqueous solution: Effect of van der Waals interactions and hybrid functionals. *The Journal of Chemical Physics*, *143*(24), 244508.

Anantharaj, S., Ede, S. R., Sakthikumar, K., Karthick, K., Mishra, S., & Kundu, S. (2016). Recent trends and perspectives in electrochemical water splitting with an emphasis on sulfide, selenide, and phosphide catalysts of Fe, Co, and Ni: A review. *Acs Catalysis*, *6*(12), 8069–8097.

Ashcroft, A. T., Cheetham, A. K., Foord, J. al, Green, M. L. H., Grey, C. P., Murrell, A. J., & Vernon, P. D. F. (1990). Selective oxidation of methane to synthesis gas using transition metal catalysts. *Nature*, *344*(6264), 319–321.

Atkins, P., Atkins, P. W., & de Paula, J. (2014). *Atkins' physical chemistry*. Oxford university press.

Avcioglu, S. G., Ozgur, E., Eroglu, I., Yucel, M., & Gunduz, U. (2011). Biohydrogen production in an outdoor panel photobioreactor on dark fermentation effluent of molasses. *International Journal of Hydrogen Energy*, *36*(17), 11360–11368.

Barducci, A., Bonomi, M., & Parrinello, M. (2011). Metadynamics. *Wiley Interdisciplinary Reviews: Computational Molecular Science*, *1*(5), 826–843.

Barnett, R. N., & Landman, U. (1993). Born-Oppenheimer molecular-dynamics simulations of finite systems: Structure and dynamics of $(H_2O)_2$. *Physical Review B*, *48*(4), 2081.

Bussi, G., Donadio, D., & Parrinello, M. (2007). Canonical sampling through velocity rescaling. *The Journal of Chemical Physics*, *126*(1), 014101.

Bussi, G., & Laio, A. (2020). Using metadynamics to explore complex free-energy landscapes. *Nature Reviews Physics*, *2*(4), 200–212.

De Levie, R. (1999). The electrolysis of water. *Journal of Electroanalytical Chemistry*, *476*(1), 92–93.

de Miranda, P. E. V. (2019). Chapter 1 - Hydrogen Energy: Sustainable and Perennial. In P. E. V. de Miranda (Ed.), *Science and Engineering of Hydrogen-Based Energy Technologies* (pp. 1–38). Academic Press. https://doi.org/10.1016/B978-0-12-814251-6.00001-0

Dey, N. K., Kim, M. J., Kim, K.-D., Seo, H. O., Kim, D., Kim, Y. D., Lim, D. C., & Lee, K. H. (2011). Adsorption and photocatalytic degradation of methylene blue over TiO_2 films on carbon fiber prepared by atomic layer deposition. *Journal of Molecular Catalysis A: Chemical*, *337*(1–2), 33–38.

Dvoranová, D., Brezová, V., Mazúr, M., & Malati, M. A. (2002). Investigations of metal-doped titanium dioxide photocatalysts. *Applied Catalysis B: Environmental*, *37*(2), 91–105. https://doi.org/10.1016/S0926-3373(01)00335-6

Escamilla-Roa, E., Timón, V., & Hernández-Laguna, A. (2012). DFT study of the adsorption of Ni on Anatase (0 0 1) surface. *Computational and Theoretical Chemistry*, *981*, 59–67.

Esswein, A. J., & Nocera, D. G. (2007). Hydrogen production by molecular photocatalysis. *Chemical Reviews*, *107*(10), 4022–4047.

Fujishima, A., & Honda, K. (1972). Electrochemical photolysis of water at a semiconductor electrode. *Nature*, *238*(5358), 37–38.

Goedecker, S., Teter, M., & Hutter, J. (1996). Separable dual-space Gaussian pseudopotentials. *Physical Review B*, *54*(3), 1703.

Goodeve, C. F., & Kitchener, J. A. (1938). The mechanism of photosensitisation by solids. *Transactions of the Faraday Society*, *34*, 902–908.

Graf, M., Mette, G., Leuenberger, D., Gurdal, Y., Iannuzzi, M., Zabka, W.-D., Schnidrig, S., Probst, B., Hutter, J., Alberto, R., & Osterwalder, J. (2017). The impact of metalation on adsorption geometry, electronic level alignment and UV-stability of organic macrocycles on TiO 2 (110). *Nanoscale*, *9*(25), 8756–8763. https://doi.org/10.1039/C7NR02317K

Guidon, M., Hutter, J., & VandeVondele, J. (2010). Auxiliary density matrix methods for Hartree- Fock exchange calculations. *Journal of Chemical Theory and Computation*, *6*(8), 2348–2364.

Guidon, M., Schiffmann, F., Hutter, J., & VandeVondele, J. (2008). Ab initio molecular dynamics using hybrid density functionals. *The Journal of Chemical Physics*, *128*(21), 214104.

Guo, X., Li, C., Wang, W., Zhang, B., Hou, Y., Wang, X., & Zhou, Q. (2021). Electronic effects on polypyridyl Co complex-based water reduction catalysts. *RSC Advances*, *11*(39), 24359–24365.

Gurdal, Y., & Iannuzzi, M. (2020). Comparison of Penta and Tetra-pyridyl Cobalt-based Catalysts for Water Reduction: H_2 Production Cycle, Solvent Response and Reduction Free Energy. *ChemPhysChem*.

Gurdal, Y., Luber, S., Hutter, J., & Iannuzzi, M. (2015). Non-innocent adsorption of Co-pyrphyrin on rutile(110). *Physical Chemistry Chemical Physics*, *17*(35), 22846–22854. https://doi.org/10.1039/C5CP02767E

Guttentag, M., Rodenberg, A., Bachmann, C., Senn, A., Hamm, P., & Alberto, R. (2012). A highly stable polypyridyl-based cobalt catalyst for homo- and heterogeneous photocatalytic water reduction. *Dalton Transactions*, *42*(2), 334–337. https://doi.org/10.1039/C2DT31699D

Guttentag, M., Rodenberg, A., Kopelent, R., Probst, B., Buchwalder, C., Brandstätter, M., Hamm, P., & Alberto, R. (2012). *Photocatalytic H_2 production with a rhenium/cobalt system in water under acidic conditions*. Wiley Online Library.

Hanaor, D. A., Assadi, M. H., Li, S., Yu, A., & Sorrell, C. C. (2012). Ab initio study of phase stability in doped TiO_2. *Computational Mechanics*, *50*(2), 185–194.

Hoffmann, P. (2019). *The forever fuel: The story of hydrogen*. Routledge.

Howard, C. J., Sabine, T. M., & Dickson, F. (1991). Structural and thermal parameters for rutile and anatase. *Acta Crystallographica Section B: Structural Science*, *47*(4), 462–468.

Humphrey, W., Dalke, A., & Schulten, K. (1996). VMD: Visual molecular dynamics. *Journal of Molecular Graphics*, *14*(1), 33–38.

Ipek, B., & Uner, D. (2019). On the limits of photocatalytic water splitting. In *Water Chemistry* (p. 177). IntechOpen.

Joliat-Wick, E., Weder, N., Klose, D., Bachmann, C., Spingler, B., Probst, B., & Alberto, R. (2018). Light-induced H_2 evolution with a macrocyclic cobalt diketo-pyrphyrin as a proton-reducing catalyst. *Inorganic Chemistry*, *57*(3), 1651–1655.

Junge, H., Codolà, Z., Kammer, A., Rockstroh, N., Karnahl, M., Luo, S.-P., Pohl, M.-M., Radnik, J., Gatla, S., & Wohlrab, S. (2014). Copper-based water reduction catalysts for efficient light-driven hydrogen generation. *Journal of Molecular Catalysis A: Chemical*, *395*, 449–456.

Koch, W., & Holthausen, M. C. (2015). *A chemist's guide to density functional theory*. John Wiley & Sons.

Kohn, W., & Sham, L. J. (1965). Self-consistent equations including exchange and correlation effects. *Physical Review*, *140*(4A), A1133.

Kutal, C. (1983). *Photochemical conversion and storage of solar energy*. ACS Publications.

Laio, A., & Parrinello, M. (2002). Escaping free-energy minima. *Proceedings of the National Academy of Sciences*, *99*(20), 12562–12566.

Leung, C.-F., Ng, S.-M., Ko, C.-C., Man, W.-L., Wu, J., Chen, L., & Lau, T.-C. (2012). A cobalt (II) quaterpyridine complex as a visible light-driven catalyst for both water oxidation and reduction. *Energy & Environmental Science*, *5*(7), 7903–7907.

LeValley, T. L., Richard, A. R., & Fan, M. (2014). The progress in water gas shift and steam reforming hydrogen production technologies–A review. *International Journal of Hydrogen Energy*, *39*(30), 16983–17000.

Li, F., Fan, K., Xu, B., Gabrielsson, E., Daniel, Q., Li, L., & Sun, L. (2015). Organic dye-sensitized tandem photoelectrochemical cell for light driven total water splitting. *Journal of the American Chemical Society*, *137*(28), 9153–9159.

Losse, S., Vos, J. G., & Rau, S. (2010). Catalytic hydrogen production at cobalt centres. *Coordination Chemistry Reviews*, *254*(21–22), 2492–2504.

Marcus, R. A. (1956). On the theory of oxidation-reduction reactions involving electron transfer. I. *The Journal of Chemical Physics*, *24*(5), 966–978.

Nikolaidis, P., & Poullikkas, A. (2017). A comparative overview of hydrogen production processes. *Renewable and Sustainable Energy Reviews*, *67*, 597–611. https://doi.org/10.1016/j.rser.2016.09.044

Perdew, J. P., Burke, K., & Ernzerhof, M. (1996). Generalized gradient approximation made simple. *Physical Review Letters*, *77*(18), 3865.

Queyriaux, N., Giannoudis, E., Windle, C. D., Roy, S., Pécaut, J., Coutsolelos, A. G., Artero, V., & Chavarot-Kerlidou, M. (2018). A noble metal-free photocatalytic system based on a novel cobalt tetrapyridyl catalyst for hydrogen production in fully aqueous medium. *Sustainable Energy & Fuels*, *2*(3), 553–557.

Reyes-Coronado, D., Rodríguez-Gattorno, G., Espinosa-Pesqueira, M. E., Cab, C., De Coss, R. D., & Oskam, G. (2008). Phase-pure TiO_2 nanoparticles: Anatase, brookite and rutile. *Nanotechnology*, *19*(14), 145605.

Rodenberg, A., Orazietti, M., Probst, B., Bachmann, C., Alberto, R., Baldridge, K. K., & Hamm, P. (2015). Mechanism of photocatalytic hydrogen generation by a polypyridyl-based cobalt catalyst in aqueous solution. *Inorganic Chemistry*, *54*(2), 646–657.

Sabatini, R., Gorni, T., & De Gironcoli, S. (2013). Nonlocal van der Waals density functional made simple and efficient. *Physical Review B*, *87*(4), 041108.

Schnidrig, S., Bachmann, C., Müller, P., Weder, N., Spingler, B., Joliat-Wick, E., Mosberger, M., Windisch, J., Alberto, R., & Probst, B. (2017). Structure–Activity and Stability Relationships for Cobalt Polypyridyl-Based Hydrogen-Evolving Catalysts in Water. *ChemSusChem*, *10*(22), 4570–4580.

Smolentsev, G., Soldatov, M. A., Probst, B., Bachmann, C., Azzaroli, N., Alberto, R., Nachtegaal, M., & van Bokhoven, J. A. (2018). Structure of the Co^{I} Intermediate of a Cobalt Pentapyridyl Catalyst for Hydrogen Evolution Revealed by Time-Resolved X-ray Spectroscopy. *ChemSusChem*, *11*(18), 3087–3091.

Su, R., Bechstein, R., Kibsgaard, J., Vang, R. T., & Besenbacher, F. (2012). High-quality Fe-doped TiO 2 films with superior visible-light performance. *Journal of Materials Chemistry*, *22*(45), 23755–23758.

Sun, Y., Bigi, J. P., Piro, N. A., Tang, M. L., Long, J. R., & Chang, C. J. (2011). Molecular cobalt pentapyridine catalysts for generating hydrogen from water. *Journal of the American Chemical Society*, *133*(24), 9212–9215.

Tong, L., Zong, R., & Thummel, R. P. (2014). Visible light-driven hydrogen evolution from water catalyzed by a molecular cobalt complex. *Journal of the American Chemical Society*, *136*(13), 4881–4884.

Turner, J. A. (2004). Sustainable hydrogen production. *Science*, *305*(5686), 972–974.

Turner, J., Sverdrup, G., Mann, M. K., Maness, P.-C., Kroposki, B., Ghirardi, M., Evans, R. J., & Blake, D. (2008). Renewable hydrogen production. *International Journal of Energy Research*, *32*(5), 379–407.

VandeVondele, J., & Hutter, J. (2007). Gaussian basis sets for accurate calculations on molecular systems in gas and condensed phases. *The Journal of Chemical Physics*, *127*(11), 114105.

VandeVondele, J., Krack, M., Mohamed, F., Parrinello, M., Chassaing, T., & Hutter, J. (2005). Quickstep: Fast and accurate density functional calculations using a mixed Gaussian and plane waves approach. *Computer Physics Communications*, *167*(2), 103–128.

Varma, S., Castillo, C. E., Stoll, T., Fortage, J., Blackman, A. G., Molton, F., Deronzier, A., & Collomb, M.-N. (2013). Efficient photocatalytic hydrogen production in water using a cobalt (III) tetraaza-macrocyclic catalyst: Electrochemical generation of the low-valent Co (I) species and its reactivity toward proton reduction. *Physical Chemistry Chemical Physics*, *15*(40), 17544–17552.

Wang, P., Liang, G., Boyd, C. L., Webster, C. E., & Zhao, X. (2019). Catalytic H_2 Evolution by a Mononuclear Cobalt Complex with a Macrocyclic Pentadentate Ligand. *European Journal of Inorganic Chemistry*, *2019*(15), 2134–2139.

Wang, P., Liang, G., Reddy, M. R., Long, M., Driskill, K., Lyons, C., Donnadieu, B., Bollinger, J. C., Webster, C. E., & Zhao, X. (2018). Electronic and steric tuning of catalytic

H_2 evolution by cobalt complexes with pentadentate polypyridyl-amine ligands. *Journal of the American Chemical Society*, *140*(29), 9219–9229.

Wang, Y., & Hwang, G. S. (2003). Adsorption of Au atoms on stoichiometric and reduced TiO_2 (1 1 0) rutile surfaces: A first principles study. *Surface Science*, *542*(1–2), 72–80.

Yang, Q., Choi, H., & Dionysiou, D. D. (2007). Nanocrystalline cobalt oxide immobilized on titanium dioxide nanoparticles for the heterogeneous activation of peroxymonosulfate. *Applied Catalysis B: Environmental*, *74*(1–2), 170–178.

Zhao, Z.-Y. (2014). Single water molecule adsorption and decomposition on the low-index stoichiometric rutile TiO_2 surfaces. *The Journal of Physical Chemistry C*, *118*(8), 4287–4295.

Zuo, Z., Huang, W., Han, P., Li, Z., & Huang, J. (2009). A DFT study on the interaction of Co with an anatase TiO2 (001)-(1$\times$ 4) surface. *Journal of Natural Gas Chemistry*, *18*(1), 78–82.